Finite element based model order reduction for parametrized one-way coupled steady state linear thermo-mechanical problems

Nirav Vasant Shah^a, Michele Girfoglio^a, Peregrina Quintela^{b,c}, Gianluigi Rozza^{a,*}, Alejandro Lengomin^d, Francesco Ballarin^e, Patricia Barral^{b,c}

^aScuola Internazionale Superiore di Studi Avanzati (SISSA), via Bonomea 265, Trieste, 34136, Italy
^bInstituto Tecnolóxico de Matemática Industrial (ITMATI), s/n, Campus Vida, Rúa de Constantino Candeira, Santiago de Compostela, 15705, Spain
^cDepartamento de Matemática Aplicada, Universidade de Santiago de Compostela, Santiago de Compostela, 15782, Spain
^dPrimary & By-Products Department, ArcelorMittal, Global R&D Asturias, P.O. Box 90, Avilés, 33400, Spain
^eDepartment of Mathematics and Physics, Catholic University of the Sacred Heart, via Musei 41, Brescia, 25121, Italy

Abstract

This contribution focuses on the development of Model Order Reduction (MOR) for one-way coupled steady state linear thermo-mechanical problems in a finite element setting. We apply Proper Orthogonal Decomposition (POD) for the computation of reduced basis space. On the other hand, for the evaluation of the modal coefficients, we use two different methodologies: the one based on the Galerkin projection (G) and the other one based on Artificial Neural Network (ANN). We aim to compare POD-G and POD-ANN in terms of relevant features including errors and computational efficiency. In this context, both physical and geometrical parametrization are considered. We also carry out a validation of the Full Order Model (FOM) based on customized benchmarks in order to provide a complete computational pipeline. The framework proposed is applied to a relevant industrial problem related to the investigation of thermo-mechanical phenomena arising in blast furnace hearth walls.

Keywords: Thermo-mechanical problems, Finite element method, Geometric and physical parametrization, Proper orthogonal decomposition, Galerkin projection, Artificial neural network, Blast furnace.

1. Introduction

Due to technological developments occurred in recent years, the high-fidelity numerical computations, based on the so-called Full Order Models (FOM) (e.g., finite element or finite volume methods), are required to be performed for many configurations. This puts the computational resources under considerable stress. In this context, Model Order Reduction (MOR) has been introduced as an efficient tool to accelerate the computations with "affordable" and "controllable" loss of accuracy. The faster computations obtained by MOR helped in many query contexts, e.g. quick transfer of computational results to industrial problems.

The basic idea on which MOR is based is related to the fact that often the parametric dependence of the problem at hand has an intrinsic dimension much lower than the number of degrees of freedom associated to the governing FOM. The development of a MOR consists in two main steps. The first one is the so-called *offline* stage when a database of several high-fidelity solutions is collected by solving the FOM for different values of physical and/or geometrical parameters. Then all the solutions are combined and compressed to extract a set of basis functions that approximate the low-dimensional manifold on which the solution lies. The second step is the *online* stage when the information obtained in the *offline* stage is used to efficiently compute the solutions for new parameters instances. For a comprehensive review on MOR, the reader is referred to, e.g., [3, 5, 7, 8, 21, 25, 38, 45].

In this work, we address the development of a MOR framework in a Finite Element (FE) environment for one-way coupled steady state linear thermo-mechanical problems. In the literature different MOR techniques have been proposed

^{*}Corresponding author

Email addresses: shah.nirav@sissa.it (Nirav Vasant Shah), michele.girfoglio@sissa.it (Michele Girfoglio), peregrina.quintela@itmati.com (Peregrina Quintela), gianluigi.rozza@sissa.it (Gianluigi Rozza), alejandro.lengomin@arcelormittal.com (Alejandro Lengomin), francesco.ballarin@unicatt.it (Francesco Ballarin), patricia.barral@usc.es (Patricia Barral)

in the context of thermo-mechanical problems. Guérin et al. [20] developed Rational Craig-Hale methodology for the investigation of thermo-mechanical coupling effects in turbomachinery. Benner et al. [6] compared the performance of Proper Orthogonal Decomposition (POD), Balanced Truncation, Padé approach and iterative rational Krylov algorithm for the approximation of the transient thermal field concerning an optimal sensor placement problem for a thermo-elastic solid body model. Zhang et al. [53] introduced reduced order variational multiscale enrichment method and tested their approach on proper benchmark tests related to the thermo-mechanical loading applied to a 2D composite beam and a functionally graded composite beam. More recently, Hernández-Beccero et al. [23] used Krylov Modal Subspace method for thermo-mechanical models as applicable to machine tools. We highlight that all these works are focused on MOR for the efficient reconstruction of the time evolution of the thermo-mechanical field. Regarding steady state problems, such as those dealt with in this work, Hoang et al. [28] used a two-field reduced basis algorithm based on the greedy algorithm in a physical parametrization setting. However, here we consider not only physical parameters but also geometrical ones. Concerning the methodology adopted, we use POD for the construction of reduced basis space. On the other hand, for the computation of the reduced coefficients, we consider two different approaches: a standard Galerkin projection (G) and Artificial Neural Network (ANN). POD-G aims to generate a MOR by a projection of the governing equations onto the POD space. So, the reduced coefficients associated to the POD bases are obtained by solving a set of algebraic equations. On the other hand, POD-ANN belongs to the category of machine learning methods based on systems that learn from data. In this framework, the reduced coefficients are computed by the employment of a properly trained neural network. There is a broad range of strategies for the development of new deep learning architectures for non-intrusive MOR approaches, i.e. without the need to access to FOM implementation: see, e.g., [24, 44, 49, 13, 36, 14, 51, 2]. We compare POD-G and POD-ANN in terms of relevant computational features including errors and speed up. From this viewpoint, the present contribution draws inspiration by [24] in which it has been shown that POD-ANN performs better than POD-G both in terms of efficiency and accuracy for steady state problems in heat transfer and fluid dynamics. We underline that whilst in [24] nonlinear problems are addressed, here we deal with a linear modeling framework by obtaining significantly different results. Our approach is applied within an industrial framework related to the investigation of thermo-mechanical phenomena arising in blast furnace hearth walls. Neural networks can in theory represent any functional relationship between inputs and output. However, many applications are still unexplored, and we retain that the use of POD-ANN method in the context of thermo-mechanical problems of industrial interest could open the door towards the application of deep learning techniques to new multiphysics scenarios.

Although the focus of this work is on the development of MOR, we dedicate a wide part of the manuscript to the FOM characterization as well as its validation in order to provide a complete computational pipeline to be used for efficient and accurate numerical simulation of thermo-mechanical problems.

The workflow of this paper is organized as follows. In Sec. 2 the physical problem related to the blast furnace hearth walls is introduced. The full order model in strong formulation is described in Sec. 3. The corresponding weak formulation is then derived in Sec. 4 and the finite element analysis is performed in Sec. 5. The validation of the full order model is presented in Sec. 6. Subsequently, in Sec. 7, the MOR approach is described and results obtained are shown and discussed. Finally, conclusions and perspectives are drawn in Sec. 8.

2. Physical problem

Steelmaking is a very old process that has contributed to the development of technological societies since ancient times. The previous stage is the ironmaking process, which is performed inside a blast furnace, whose general layout is shown in Figure 1. It is a metallurgical reactor used to produce hot metal from iron ore. For further details the reader is referred, e.g., to [11, 17].

The blast furnace operates at a high temperature (up to 1500 °C). The associated thermal stresses significantly limit the overall blast furnace campaign period. In this context, thermo-mechanical modeling has been used extensively either to support experimental campaign or to design various components. Vázquez-Fernández et al. [50] simulated heat transfer in a trough of a blast furnace to ensure durability based on the location of critical isotherm. Numerical modeling of heat flows in the blast furnace hearth lining was used by Swartling M. et al. [48] for improving experimental assessment. Thermo-mechanical modeling of blast furnace hearth was also developed by Brulin et al. [10]: they used micro-macro approach with homogenization method for replacing bricks and mortars by an equivalent material.

The blast furnace operates under different conditions, each of which is governed by a different mathematical model. Considering the objectives of the present work, the following simplifications are considered:

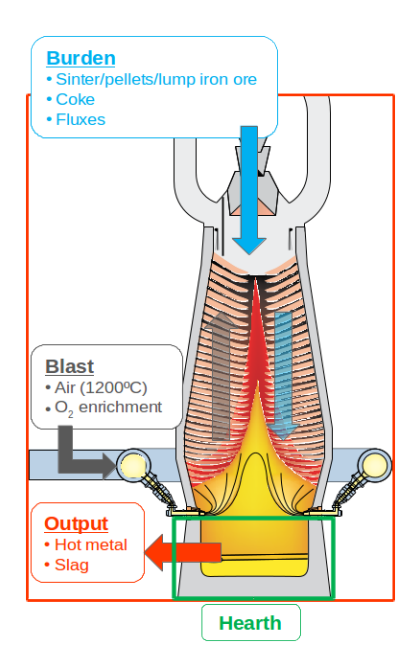


Figure 1: Blast furnace [Courtesy: ArcelorMittal, Spain].

- Taphole operation is not part of this study. The perforation action of the taphole and the important pressures in the draining of the hot metal and slag produce important mechanical stresses located in the area that requires a deeper analysis and that is out of the scope of this work.
- Since the objective is to be able to calculate in real time the effects of wall design on blast furnace operation, we focus on the steady state operations.
- We assume that the hearth is made up of a single homogeneous, elastic, and isotropic material with temperature-independent material properties.
- Heat transfer only by conduction within hearth walls will be considered. The temperature of the molten metal inside the hearth is assumed constant and known. Therefore, the fluid region will not be part of the problem.

3. Full order model

In this section, we discuss the mathematical formulation corresponding to the physical problem described in Sec.

- 2. The strong formulation of the governing equations endowed with suitable boundary conditions is reported in Sec.
- 3.1. Then, we derive the thermo-mechanical model in cylindrical coordinates in Sec. 3.2. Finally, we introduce the axisymmetric hypothesis and derive the axisymmetric thermo-mechanical model in Sec. 3.3.

3.1. Energy and momentum conservation equations

We consider the three dimensional domain Ω as in Figure 2 (b), corresponding to the simplified hearth geometry. We represent the displacement vector field as \overrightarrow{u} and the temperature scalar field as T. Based on the simplifications listed in Sec. 2, the energy and momentum conservation equations can be written respectively as [12, 18, 19],

$$-\operatorname{Div}(\mathbf{K}\nabla T) = Q \text{ in } \Omega, \tag{1}$$

$$-\operatorname{Div}(\boldsymbol{\sigma}) = \overrightarrow{f_0} \text{ in } \Omega . \tag{2}$$

Here, \overrightarrow{f}_0 is the body force density term, Q is the heat source term and K is the thermal conductivity tensor. In the case of isotropic material, the thermal conductivity K is expressed as,

$$\mathbf{K} = k\mathbf{I} \quad \text{with } k > 0 \,, \tag{3}$$

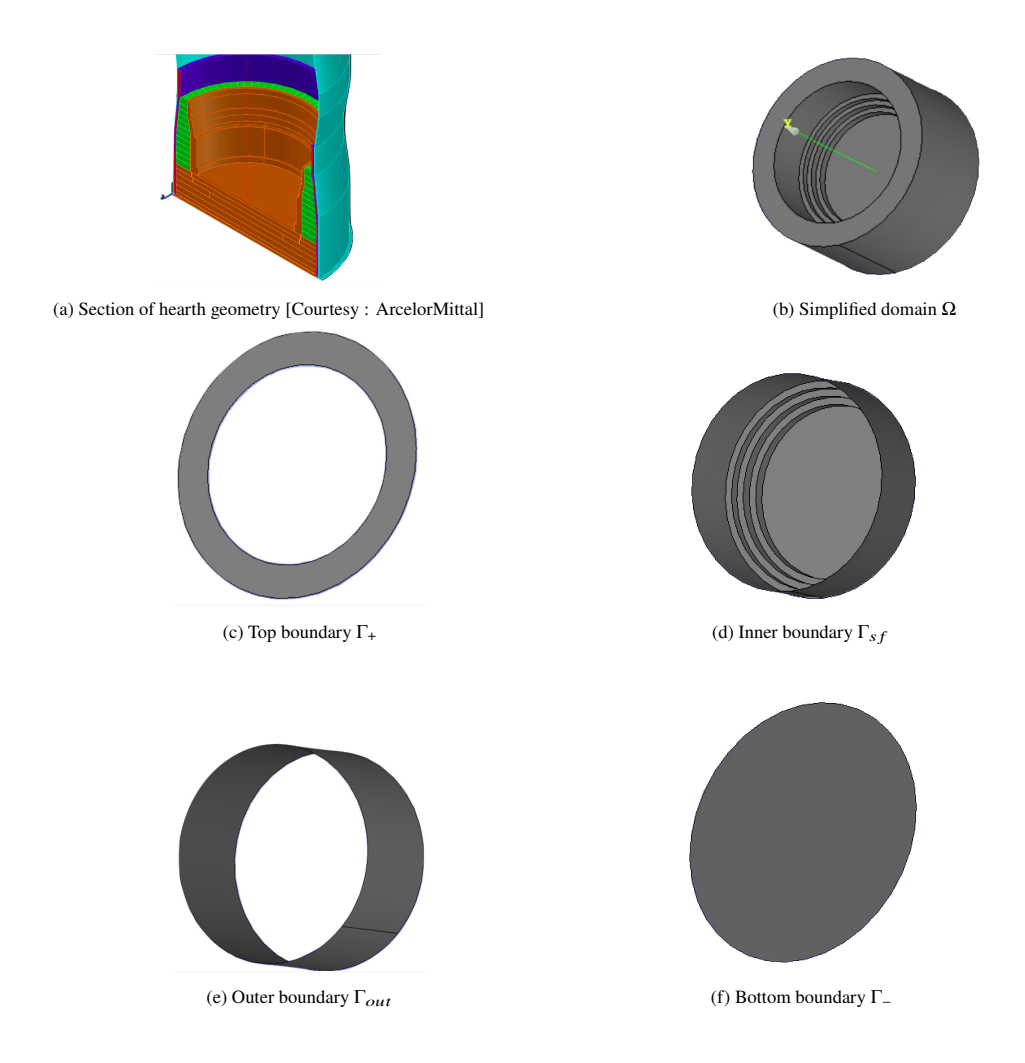


Figure 2: Hearth geometry: three dimensional domains, the real one (a) and its simplification (b), as well as its boundaries (c-f).

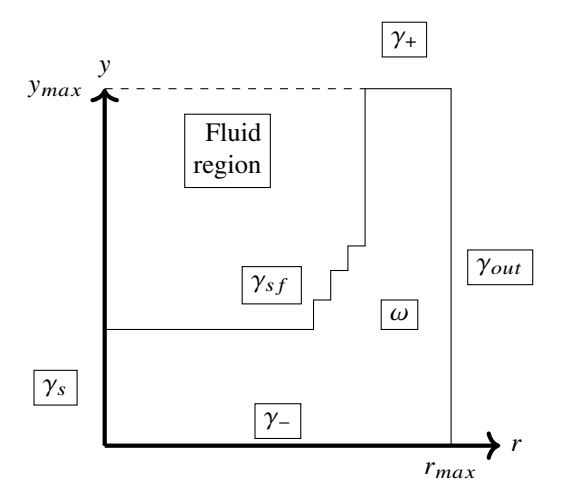


Figure 3: Vertical section of the computational domain and its boundaries.

where I refers to the identity tensor.

The thermo-mechanical stress tensor σ is related to the strain tensor ε through the Hooke's law:

$$\sigma(\overrightarrow{u})[T] = \lambda \operatorname{Tr}(\varepsilon(\overrightarrow{u}))I + 2\mu\varepsilon(\overrightarrow{u}) - (2\mu + 3\lambda)\alpha(T - T_0)I, \qquad (4)$$

where T_0 is the reference temperature, ε is defined as,

$$\varepsilon(\overrightarrow{u}) = \frac{1}{2} (\nabla \overrightarrow{u} + \nabla \overrightarrow{u}^T) , \qquad (5)$$

 α is the thermal expansion coefficient, and λ and μ are the Lamé parameters of the material. These latter can be expressed in terms of Young modulus, E, and Poisson ratio, ν , as:

$$\mu = \frac{E}{2(1+\nu)} , \ \lambda = \frac{E\nu}{(1-2\nu)(1+\nu)} . \tag{6}$$

As will be discussed in Sec. 3.3, the simplifications assumed allow us to consider that Ω has axial symmetry. Then, the equations (1)-(2) will be solved on its vertical section, ω , shown in Figure 3.

3.1.1. Boundary conditions

We introduce the notations for the boundaries of the domain Ω (Figure 2), and its vertical cross section in r-y plane, ω (Figure 3):

$$\Gamma_{out} = \partial\Omega \cap (r \equiv r_{max}) = \gamma_{out} \times [0, 2\pi) ,$$

$$\Gamma_{+} = \partial\Omega \cap (y \equiv y_{max}) = \gamma_{+} \times [0, 2\pi) ,$$

$$\Gamma_{-} = \partial\Omega \cap (y \equiv 0) = \gamma_{-} \times [0, 2\pi) ,$$

$$\Gamma_{sf} = \partial\Omega \setminus (\Gamma_{out} \cup \Gamma_{+} \cup \Gamma_{-}) = \gamma_{sf} \times [0, 2\pi) ,$$

$$\gamma_{s} = \partial\omega \cap (r \equiv 0) ,$$

$$(7)$$

where $r_{max} \in \mathbb{R}^+$ and $y_{max} \in \mathbb{R}^+$.

Moreover, on the boundary, we define normal force σ_n and tangential force $\overrightarrow{\sigma_t}$ as follows:

$$\sigma_n = (\overrightarrow{\sigma n}) \cdot \overrightarrow{n} ,$$

$$\overrightarrow{\sigma_t} = \overrightarrow{\sigma n} - \sigma_n \overrightarrow{n} ,$$
(8)

where \overrightarrow{n} is the unit normal vector that is directed outwards from Ω .

• On the upper boundary, Γ_+ , the applied force, \overrightarrow{g}_+ , and the density of heat flux, q_+ , are known. Therefore, the following boundary conditions are considered:

$$(-K\nabla T) \cdot \overrightarrow{n} = q_+,$$

$$\sigma \overrightarrow{n} = \overrightarrow{g}_+.$$
(9)

• On the bottom boundary, Γ_- , the convection heat transfer occurs with the heat exchanger at temperature T_- and heat transfer coefficient $h_{c,-}$. The normal displacement is null, and we denote with \overrightarrow{g}_- the shear force. Therefore, it is verified:

$$(-K\nabla T) \cdot \overrightarrow{n} = h_{c,-}(T - T_{-}),$$

$$\overrightarrow{u} \cdot \overrightarrow{n} = 0,$$

$$\overrightarrow{\sigma_t} = \overrightarrow{g}_{-}.$$
(10)

• On the inner boundary, Γ_{sf} , convection heat transfer with the fluid phase occurs and hydrostatic pressure g_{sf} is acting. So, the following boundary conditions are considered:

$$(-K\nabla T) \cdot \overrightarrow{n} = h_{c,f} (T - T_f) ,$$

$$\sigma \overrightarrow{n} = \overrightarrow{g}_{sf} ,$$
(11)

where T_f is the fluid temperature, assumed to be known and constant at the steady state, and $h_{c,f}$ is the convective heat transfer coefficient. In addition, $\overrightarrow{g}_{sf} = -g_{sf} \overrightarrow{n}$.

• On the outer boundary, Γ_{out} , a convective heat flux and known applied force \overrightarrow{g}_{out} are assumed:

$$(-K\nabla T) \cdot \overrightarrow{n} = h_{c,out}(T - T_{out}) ,$$

$$\sigma \overrightarrow{n} = \overrightarrow{g}_{out} ,$$
(12)

 $h_{c,out}$ being the convective heat transfer coefficient and T_{out} the ambient temperature.

3.2. Thermo-mechanical model in cylindrical coordinates

We are going to express the governing equations (1) and (2), and boundary conditions (9)-(12), in a cylindrical coordinates system, (r, y, θ) , with $(r, y) \in \omega$ (see Figure 3), and $\theta \in [0, 2\pi)$.

Assuming (3), the energy conservation equation (1) can be rewritten as:

$$-\frac{1}{r}\frac{\partial}{\partial r}\left(rk\frac{\partial T}{\partial r}\right) - \frac{\partial}{\partial y}\left(k\frac{\partial T}{\partial y}\right) - \frac{1}{r}\frac{\partial}{\partial \theta}\left(\frac{k}{r}\frac{\partial T}{\partial \theta}\right) = Q, \text{ in } \Omega.$$
(13)

The corresponding thermal boundary conditions (9)-(12) are

on
$$\Gamma_{+}: (-k\nabla T) \cdot \overrightarrow{n} = q_{+}$$
,
on $\Gamma_{-}: (-k\nabla T) \cdot \overrightarrow{n} = h_{c,-}(T - T_{-})$,
on $\Gamma_{sf}: (-k\nabla T) \cdot \overrightarrow{n} = h_{c,f}(T - T_{f})$,
on $\Gamma_{out}: (-k\nabla T) \cdot \overrightarrow{n} = h_{c,out}(T - T_{out})$.

On the other hand, the momentum conservation equation (2) corresponds to the three following equations:

$$\frac{\partial \sigma_{rr}}{\partial r} + \frac{\partial \sigma_{ry}}{\partial y} + \frac{1}{r} \frac{\partial \sigma_{r\theta}}{\partial \theta} + \frac{\sigma_{rr} - \sigma_{\theta\theta}}{r} + f_{0,r} = 0 , \text{ in } \Omega ,$$

$$\frac{\partial \sigma_{r\theta}}{\partial r} + \frac{\partial \sigma_{\theta y}}{\partial y} + \frac{1}{r} \frac{\partial \sigma_{\theta\theta}}{\partial \theta} + 2 \frac{\sigma_{r\theta}}{r} + f_{0,\theta} = 0 , \text{ in } \Omega ,$$

$$\frac{\partial \sigma_{ry}}{\partial r} + \frac{1}{r} \frac{\partial \sigma_{\theta y}}{\partial \theta} + \frac{\partial \sigma_{yy}}{\partial y} + \frac{\sigma_{ry}}{r} + f_{0,y} = 0 , \text{ in } \Omega .$$
(15)

The corresponding mechanical boundary conditions (9)-(12) are:

on
$$\Gamma_{+}$$
: $\overrightarrow{\sigma n} = \overrightarrow{g}_{+}$,
on Γ_{-} : $\overrightarrow{u} \cdot \overrightarrow{n} = 0$, $\overrightarrow{\sigma_{t}} = \overrightarrow{g}_{-}$,
on Γ_{sf} : $\overrightarrow{\sigma n} = \overrightarrow{g}_{sf}$,
on Γ_{out} : $\overrightarrow{\sigma n} = \overrightarrow{g}_{out}$. (16)

The strain tensor in cylindrical coordinate system (r, y, θ) is given by,

$$\varepsilon(\overrightarrow{u}) = \begin{bmatrix} \frac{\partial u_r}{\partial r} & \frac{1}{2} \left(\frac{\partial u_r}{\partial y} + \frac{\partial u_y}{\partial r} \right) & \frac{1}{2} \left(\frac{\partial u_\theta}{\partial r} + \frac{1}{r} \frac{\partial u_r}{\partial \theta} - \frac{u_\theta}{r} \right) \\ \frac{1}{2} \left(\frac{\partial u_r}{\partial y} + \frac{\partial u_y}{\partial r} \right) & \frac{\partial u_y}{\partial y} & \frac{1}{2r} \left(\frac{\partial u_y}{\partial \theta} + r \frac{\partial u_\theta}{\partial y} \right) \\ \frac{1}{2} \left(\frac{\partial u_\theta}{\partial r} + \frac{1}{r} \frac{\partial u_r}{\partial \theta} - \frac{u_\theta}{r} \right) & \frac{1}{2r} \left(\frac{\partial u_y}{\partial \theta} + r \frac{\partial u_\theta}{\partial y} \right) & \frac{1}{r} \frac{\partial u_\theta}{\partial \theta} + \frac{u_r}{r} \end{bmatrix}.$$

$$(17)$$

If A denotes the fourth order tensor defined as:

$$A = \frac{E}{(1-2\nu)(1+\nu)} \begin{bmatrix} 1-\nu & \nu & \nu & 0 & 0 & 0\\ \nu & 1-\nu & \nu & 0 & 0 & 0\\ \nu & \nu & 1-\nu & 0 & 0 & 0\\ 0 & 0 & 0 & \frac{1-2\nu}{2} & 0 & 0\\ 0 & 0 & 0 & 0 & \frac{1-2\nu}{2} & 0\\ 0 & 0 & 0 & 0 & 0 & \frac{1-2\nu}{2} \end{bmatrix},$$
(18)

stress-strain relationship can be expressed in vector formulation as,

$$\{\sigma(\overrightarrow{u})[T]\} = A\{\varepsilon(\overrightarrow{u})\} - (2\mu + 3\lambda)\alpha(T - T_0)\{I\}, \tag{19}$$

where the following column vectors have been considered:

$$\{\boldsymbol{\sigma}\} = \{\boldsymbol{\sigma}_{rr} \quad \boldsymbol{\sigma}_{yy} \quad \boldsymbol{\sigma}_{\theta\theta} \quad \boldsymbol{\sigma}_{y\theta} \quad \boldsymbol{\sigma}_{r\theta} \quad \boldsymbol{\sigma}_{ry}\}^{T},$$

$$\{\boldsymbol{\varepsilon}\} = \{\boldsymbol{\varepsilon}_{rr} \quad \boldsymbol{\varepsilon}_{yy} \quad \boldsymbol{\varepsilon}_{\theta\theta} \quad 2\boldsymbol{\varepsilon}_{y\theta} \quad 2\boldsymbol{\varepsilon}_{r\theta} \quad 2\boldsymbol{\varepsilon}_{ry}\}^{T},$$

$$\{\boldsymbol{I}\} = \{1 \quad 1 \quad 1 \quad 0 \quad 0 \quad 0\}^{T}.$$

$$(20)$$

3.3. Axisymmetric thermo-mechanical model

In the context of blast furnace application, the body force density term $\overrightarrow{f_0}$, as well as surface forces, \overrightarrow{g}_+ , \overrightarrow{g}_- , \overrightarrow{g}_{sf} , \overrightarrow{g}_{out} , have zero component in $\overrightarrow{e_\theta}$ direction and they do not depend on θ . Besides, the heat source term, Q, the heat flux density, q_+ , the heat transfer coefficients, $h_{c,-}$, $h_{c,out}$, and temperatures T_- , T_f , T_{out} are assumed to be only dependent on (r,y) coordinates. Therefore, a symmetry hypothesis is applicable that leads to significant computational savings.

The associated axisymmetric model is reduced to consider conservation equations (13), (15) defined in ω and the boundary conditions (14), (16), where the Γ boundaries are replaced by γ such that $\Gamma = (\gamma \setminus \gamma_s) \times [0, 2\pi)$ (see Figures 2 and 3, and definitions (7)). Moreover, the usual symmetry conditions on γ_s are added:

$$(-k\nabla T) \cdot \overrightarrow{n} = 0,$$

$$\overrightarrow{u} \cdot \overrightarrow{n} = 0,$$

$$\overrightarrow{\sigma_t} = \overrightarrow{0}.$$
(21)

In vector notation, axisymmetric stress-strain relationship and elasticity matrix A, defined in equation (18), can be expressed as,

$$\{\boldsymbol{\sigma}(\overrightarrow{u})[T]\} = A\{\boldsymbol{\varepsilon}(\overrightarrow{u})\} - (2\mu + 3\lambda)\alpha(T - T_0)\{I\},$$

$$A = \frac{E}{(1 - 2\nu)(1 + \nu)} \begin{bmatrix} 1 - \nu & \nu & \nu & 0 \\ \nu & 1 - \nu & \nu & 0 \\ \nu & \nu & 1 - \nu & 0 \\ 0 & 0 & 0 & \frac{1 - 2\nu}{2} \end{bmatrix},$$

$$\{\boldsymbol{\sigma}\} = \{\boldsymbol{\sigma}_{rr} \quad \boldsymbol{\sigma}_{yy} \quad \boldsymbol{\sigma}_{\theta\theta} \quad \boldsymbol{\sigma}_{ry}\}^{T},$$

$$\{\boldsymbol{\varepsilon}\} = \{\boldsymbol{\varepsilon}_{rr} \quad \boldsymbol{\varepsilon}_{yy} \quad \boldsymbol{\varepsilon}_{\theta\theta} \quad 2\boldsymbol{\varepsilon}_{ry}\}^{T},$$

$$\{I\} = \{1 \quad 1 \quad 1 \quad 0\}^{T}.$$

$$(22)$$

Therefore, the axisymmetric thermo-mechanical model can be summarized as:

· Thermal model:

$$-\frac{1}{r}\frac{\partial}{\partial r}\left(rk\frac{\partial T}{\partial r}\right) - \frac{\partial}{\partial y}\left(k\frac{\partial T}{\partial y}\right) = Q, \text{ in } \omega,$$
(23)

with boundary conditions:

on
$$\gamma_{+}$$
: $-k\frac{\partial T}{\partial y} = q_{+}$,
on γ_{-} : $k\frac{\partial T}{\partial y} = h_{c,-}(T - T_{-})$,
on γ_{sf} : $-k\frac{\partial T}{\partial r}n_{r} - k\frac{\partial T}{\partial y}n_{y} = h_{c,f}(T - T_{f})$,
on γ_{out} : $-k\frac{\partial T}{\partial r} = h_{c,out}(T - T_{out})$,
on γ_{s} : $\frac{\partial T}{\partial r} = 0$.

• Mechanical model:

$$\frac{\partial \sigma_{rr}}{\partial r} + \frac{\partial \sigma_{ry}}{\partial y} + \frac{\sigma_{rr} - \sigma_{\theta\theta}}{r} + f_{0,r} = 0, \text{ in } \omega,
\frac{\partial \sigma_{ry}}{\partial r} + \frac{\partial \sigma_{yy}}{\partial y} + \frac{\sigma_{ry}}{r} + f_{0,y} = 0, \text{ in } \omega,$$
(25)

with the boundary conditions:

on
$$\gamma_{+}$$
: $\sigma_{ry} = g_{+,r}$, $\sigma_{yy} = g_{+,y}$,
on γ_{-} : $u_{y} = 0$, $\sigma_{ry} = -g_{-,r}$,
on γ_{sf} : $\sigma_{rr}n_{r} + \sigma_{ry}n_{y} = g_{sf,r}$,
 $\sigma_{ry}n_{r} + \sigma_{yy}n_{y} = g_{sf,y}$,
on γ_{out} : $\sigma_{rr} = g_{out,r}$, $\sigma_{ry} = g_{out,y}$,
on γ_{s} : $u_{r} = 0$, $\sigma_{ry} = 0$.

4. Weak formulation of axisymmetric thermo-mechanical model

In this section, we derive the weak formulation related to the axisymmetric thermo-mechanical model (23)-(26). First, in Sec. 4.1, we introduce the relevant function spaces for temperature and displacement fields as well as for the model data, including boundary conditions, physical properties, and source terms, such that the problem is well defined. Next, the weak formulations for the thermal and mechanical problems are reported in Sec. 4.2 and 4.3, respectively.

4.1. Functional spaces

For data of both thermal and mechanical problem, we introduce the weighted Sobolev spaces, $L_r^2(\omega)$, with norm $||\cdot||_{L_r^2(\omega)}$ as,

$$L_r^2(\omega) = \left\{ f : \omega \mapsto \mathbb{R} , \int_{\omega} f^2 r dr dy < \infty \right\},$$

$$||f||_{L_r^2(\omega)}^2 = \int_{\omega} f^2 r dr dy.$$
(27)

Analogously, given γ a subset of $\partial \omega$, the boundary of ω ,

$$L_r^2(\gamma) = \left\{ g : \gamma \mapsto \mathbb{R}, \int_{\gamma} g^2 r d\gamma < \infty \right\}. \tag{28}$$

Let $L^{\infty}(\omega)$ be the space

$$L^{\infty}(\omega) = \{ f : \omega \mapsto \mathbb{R}, \sup_{\omega} |f| \le C, C \ge 0 \},$$
$$||f||_{L^{\infty}(\omega)} = \sup_{\omega} |f|.$$
 (29)

Analogously, $L^{\infty}(\gamma)$ is defined.

For the temperature, we introduce the weighted Sobolev space, $H_r^1(\omega)$, with norm $||\cdot||_{H_r^1(\omega)}$ as,

$$H_{r}^{1}(\omega) = \left\{ \psi : \omega \mapsto \mathbb{R} , \int_{\omega} \left(\psi^{2} + \left(\frac{\partial \psi}{\partial r} \right)^{2} + \left(\frac{\partial \psi}{\partial y} \right)^{2} \right) r dr dy < \infty \right\},$$

$$||\psi||_{H_{r}^{1}(\omega)}^{2} = \int_{\omega} \left(\psi^{2} + \left(\frac{\partial \psi}{\partial r} \right)^{2} + \left(\frac{\partial \psi}{\partial y} \right)^{2} \right) r dr dy.$$

$$(30)$$

On the other hand, the following space V for the displacement is considered:

$$\mathbb{V} = (H_r^1(\omega) \cap L_{1/r}^2(\omega)) \times H_r^1(\omega) . \tag{31}$$

It will be equipped with the inner product,

$$<\overrightarrow{u},\overrightarrow{\phi}>_{\mathbb{V}}=\int_{\omega}\left(\phi_{r}u_{r}+\phi_{y}u_{y}+\frac{\partial u_{r}}{\partial r}\frac{\partial\phi_{r}}{\partial r}+\frac{\partial u_{r}}{\partial y}\frac{\partial\phi_{r}}{\partial y}+\frac{u_{r}}{r}\frac{\phi_{r}}{r}+\frac{\partial u_{y}}{\partial r}\frac{\partial\phi_{y}}{\partial r}+\frac{\partial u_{y}}{\partial y}\frac{\partial\phi_{y}}{\partial y}+\frac{\partial u_{r}}{\partial y}\frac{\partial\phi_{y}}{\partial r}+\frac{\partial u_{y}}{\partial y}\frac{\partial\phi_{y}}{\partial r}+\frac{\partial u_{y}}{\partial r}\frac{\partial\phi_{y}}{\partial r}+\frac{\partial u_{y}}{\partial r}\frac{\partial\phi_{y}$$

(32)

and with the norm,

$$||\overrightarrow{\phi}||_{\mathbb{V}}^{2} = \langle \overrightarrow{\phi}, \overrightarrow{\phi} \rangle_{\mathbb{V}} . \tag{33}$$

Its closed and convex subspace U,

$$\mathbb{U} = \{ \overrightarrow{\phi} = (\phi_r \ \phi_y) \in \mathbb{V} \ , \ \phi_y = 0 \text{ on } \gamma_- \ , \ \phi_r = 0 \text{ on } \gamma_s \ \} \ , \tag{34}$$

will be the set of admissible displacements. The subspace \mathbb{U} is equipped with the same norm as spave \mathbb{V} i.e. $||\overrightarrow{\phi}||_{\mathbb{U}} = ||\overrightarrow{\phi}||_{\mathbb{V}}, \forall \overrightarrow{\phi} \in \mathbb{U}$.

Finally, the function space for stress tensor is defined as,

$$\mathbb{S} = \{ \boldsymbol{\sigma} = [\sigma_{ij}] \in [L_r^2(\omega)]^{3 \times 3}, \sigma_{ij} = \sigma_{ii}, \sigma_{\alpha 3} = 0, \alpha = 1, 2 \}.$$
 (35)

For more details the reader is referred, e.g., to [26, 27, 31].

4.2. Weak formulation for thermal model

We assume the following hypotheses on the data:

(TH1) The heat source term, Q, is such that

$$Q \in L_r^2(\omega)$$
.

(TH2) The convection temperatures, T_{sf} , T_{-} and T_{out} , as well as the boundary heat flux q_{+} are such that

$$T_{sf}\in L^2_r(\gamma_{sf})$$
 , $T_-\in L^2_r(\gamma_-)$, $T_{out}\in L^2_r(\gamma_{out})$, $q_+\in L^2_r(\gamma_+)$.

(TH3) The thermal conductivity k(r, y) and the convective heat transfer coefficients, $h_{c,f}(r, y)$, $h_{c,out}(r, y)$ and $h_{c,-}(r, y)$ are such that

$$k(r, y) \in L^{\infty}(\omega) , k(r, y) > k_{0} > 0 ,$$

$$h_{c,f}(r, y) \in L^{\infty}(\gamma_{sf}) , h_{c,f}(r, y) > h_{c,f,0} > 0 ,$$

$$h_{c,out}(r, y) \in L^{\infty}(\gamma_{out}) , h_{c,out}(r, y) > h_{c,out,0} > 0 ,$$

$$h_{c,-}(r, y) \in L^{\infty}(\gamma_{-}) , h_{c,-}(r, y) > h_{c,-0} > 0 ,$$

where k_0 , $h_{c,f,0}$, $h_{c,out,0}$ and $h_{c,-,0}$ are suitable constants.

In order to propose a weak formulation for the thermal model (23) - (24), in the following we assume sufficient regularity to perform the calculations. We multiply the energy equation (23) by $r\psi(r, y)$, integrate over the domain ω with respect to (r, y) variables, apply Gauss divergence theorem and use boundary conditions (24) to obtain:

$$\int_{\omega} rk \left(\frac{\partial T}{\partial y} \frac{\partial \psi}{\partial y} + \frac{\partial T}{\partial r} \frac{\partial \psi}{\partial r} \right) dr dy + \int_{\gamma_{sf}} \psi h_{c,f} Tr d\gamma + \int_{\gamma_{out}} \psi h_{c,out} Tr d\gamma + \int_{\gamma_{-}} \psi h_{c,-} Tr d\gamma = \int_{\omega} \psi Qr dr dy + \int_{\gamma_{sf}} \psi h_{c,f} T_{f} r d\gamma + \int_{\gamma_{out}} \psi h_{c,out} T_{out} r d\gamma + \int_{\gamma_{-}} \psi h_{c,-} T_{-} r d\gamma - \int_{\gamma_{+}} \psi q^{+} r d\gamma .$$
(36)

It is to be noted that under assumptions (TH1)-(TH3) all integrals of the proposed weak formulation are well defined for all $T, \psi \in H^1_r(\omega)$. The left hand side of equation (36) is bilinear and symmetric. So, we define in $H^1_r(\omega) \times H^1_r(\omega)$ the operator:

$$a_{T}(T,\psi) = \int_{\omega} rk \left(\frac{\partial T}{\partial y} \frac{\partial \psi}{\partial y} + \frac{\partial T}{\partial r} \frac{\partial \psi}{\partial r} \right) dr dy + \int_{\gamma_{sf}} \psi h_{c,f} Tr d\gamma + \int_{\gamma_{out}} \psi h_{c,out} Tr d\gamma + \int_{\gamma} \psi h_{c,-} Tr d\gamma .$$

$$(37)$$

The right hand side of equation (36) is linear and the following operator defined on $H_r^1(\omega)$ is introduced:

$$l_{T}(\psi) = \int_{\omega} \psi Q r dr dy + \int_{\gamma_{sf}} \psi h_{c,f} T_{f} r d\gamma + \int_{\gamma_{out}} \psi h_{c,out} T_{out} r d\gamma + \int_{\gamma_{-}} \psi h_{c,-} T_{-} r d\gamma - \int_{\gamma_{+}} \psi q^{+} r d\gamma .$$

$$(38)$$

Then, we can define the following problem:

• Weak thermal model (WT): Under the assumptions (TH1)-(TH3), find $T \in H_r^1(\omega)$ such that,

$$a_T(T, \psi) = l_T(\psi), \ \forall \ \psi \in H^1_r(\omega).$$
 (39)

By using Cauchy-Schwarz inequality, the trace operator properties, and Friedrich's inequality [9, 34], it can be shown that, under the assumptions (TH1)-(TH3), $a_T(T,\psi)$ and $l_T(\psi)$ are continuous on $H^1_r(\omega) \times H^1_r(\omega)$ and $H^1_r(\omega)$, respectively, and $a_T(\psi,\psi)$ is coercive on $H^1_r(\omega) \times H^1_r(\omega)$. Hence the conditions of the Lax-Milgram theorem [9] are satisfied and accordingly the weak thermal model (WT) has a unique solution.

4.3. Weak formulation of the mechanical model

We assume the following hypotheses on the data:

(MH1) The body force density, $\overrightarrow{f_0}$, is such that

$$\overrightarrow{f_0} \in [L_r^2(\omega)]^2$$
.

(MH2) The boundary forces \overrightarrow{g}_+ , \overrightarrow{g}_{sf} , \overrightarrow{g}_{out} and \overrightarrow{g}_- are such that

$$\overrightarrow{g}_{+} \in [L_{r}^{2}(\gamma_{+})]^{2}, \overrightarrow{g}_{sf} \in [L_{r}^{2}(\gamma_{sf})]^{2}, \overrightarrow{g}_{out} \in [L_{r}^{2}(\gamma_{out})]^{2}, \overrightarrow{g}_{-} \in [L_{r}^{2}(\gamma_{-})]^{2}.$$

(MH3) The Young's modulus E(r, y), the coefficient of thermal expansion $\alpha(r, y)$, and the Poisson's ratio $\nu(r, y)$ are such that

$$E(r, y) \in L^{\infty}(\omega), E > E_0 > 0,$$

 $\alpha(r, y) \in L^{\infty}(\omega), \alpha > \alpha_0 > 0,$
 $\nu(r, y) \in L^{\infty}(\omega), \nu_0 < \nu < \nu_1, \nu_0 > 0,$

where E_0 , α_0 , ν_0 and ν_1 are suitable constants.

Analogously to what has been done for the thermal model, to propose a weak formulation of the mechanical model (25) - (26), in the following we assume sufficient regularity to perform the calculations. Given a function $\overrightarrow{\phi} = (\phi_r, \phi_y)$, we multiply the first equation of (25) by $r\phi_r(r, y)$, the second one by $r\phi_y(r, y)$, we sum both, integrate over ω , apply Green formula and use equation (4) and (26) to obtain

$$\int_{\omega} A\{\boldsymbol{\varepsilon}(\overrightarrow{u})\} \cdot \{\boldsymbol{\varepsilon}(\overrightarrow{\phi})\} r dr dy = \int_{\omega} (2\mu + 3\lambda)\alpha (T - T_{0})\{\boldsymbol{I}\} \cdot \{\boldsymbol{\varepsilon}(\overrightarrow{\phi})\} r dr dy + \int_{\omega} (\phi_{r} f_{0,r} + \phi_{y} f_{0,y}) r dr dy + \int_{\gamma_{sf}} \overrightarrow{\phi} \cdot \overrightarrow{g}_{sf} r d\gamma + \int_{\gamma_{out}} \overrightarrow{\phi} \cdot \overrightarrow{g}_{out} r d\gamma + \int_{\gamma_{-}} \overrightarrow{\phi} \cdot \overrightarrow{g}_{-} r d\gamma + \int_{\gamma_{+}} \overrightarrow{\phi} \cdot \overrightarrow{g}_{+} r d\gamma , \forall \overrightarrow{u}, \overrightarrow{\phi} \in \mathbb{U} ,$$

$$(40)$$

where T is assumed to be the solution of the weak thermal model (WT).

Notice that under assumptions (MH1)-(MH3), and since $T \in H_r^1(\omega)$, all integrals in (40) are well defined for all \overrightarrow{u} , $\overrightarrow{\phi} \in \mathbb{U}$.

The left hand side of equation (40),

$$a_{M}(\overrightarrow{u}, \overrightarrow{\phi}) = \int_{\omega} A\{\varepsilon(\overrightarrow{u})\} \cdot \{\varepsilon(\overrightarrow{\phi})\} r dr dy, \qquad (41)$$

is bilinear in $\mathbb{V} \times \mathbb{V}$, while the right hand side,

$$l_{M}[T](\overrightarrow{\phi}) = \int_{\omega} (2\mu + 3\lambda)\alpha(T - T_{0})\{I\} \cdot \{\varepsilon(\overrightarrow{\phi})\}rdrdy + \int_{\omega} (\phi_{r}f_{0,r} + \phi_{y}f_{0,y})rdrdy + \int_{\gamma_{out}} \overrightarrow{\phi} \cdot \overrightarrow{g}_{sf}rd\gamma + \int_{\gamma_{out}} \overrightarrow{\phi} \cdot \overrightarrow{g}_{out}rd\gamma + \int_{\gamma_{-}} \overrightarrow{\phi} \cdot \overrightarrow{g}_{-}rd\gamma + \int_{\gamma_{+}} \overrightarrow{\phi} \cdot \overrightarrow{g}_{+}rd\gamma ,$$

$$(42)$$

is linear in V. By using these two operators, the weak formulation of the mechanical problem can be expressed as follows:

• Weak mechanical problem (WM): Let $T \in H^1_r(\omega)$ be the solution of the weak thermal model (WT). Under the assumptions (MH1)-(MH3), find $\overrightarrow{u} \in \mathbb{U}$ such that,

$$a_{M}(\overrightarrow{u}, \overrightarrow{\phi}) = l_{M}[T](\overrightarrow{\phi}), \ \forall \overrightarrow{\phi} \in \mathbb{U}.$$
 (43)

By using Lemmas 2.2 and 2.3 of [27], under the assumption (MH3), one can show that $a_M(\overrightarrow{u}, \overrightarrow{\phi})$ and $l_M[T](\overrightarrow{\phi})$ are continuous in $\mathbb{V} \times \mathbb{V}$ and \mathbb{V} , respectively, and a_M is \mathbb{U} -coercive. Hence the conditions of the Lax-Milgram theorem are satisfied and accordingly the weak mechanical formulation (WM) has a unique solution.

Notice that here we could use the principle of superposition: the net displacement at any point in the domain \overrightarrow{u} is the sum of the displacement due to purely mechanical effects $\overrightarrow{u}_M \in \mathbb{U}$ and the displacement due to purely thermal effects $\overrightarrow{u}_T \in \mathbb{U}$:

$$\overrightarrow{u} = \overrightarrow{u}_M + \overrightarrow{u}_T . \tag{44}$$

Therefore, the problem (WM) could be split in two sub-problems:

• Weak mechanical problem (WM1): Under the assumptions (MH1)-(MH3), find $\overrightarrow{u}_M \in \mathbb{U}$ such that,

$$a_{M}(\overrightarrow{u}_{M}, \overrightarrow{\phi}) = l_{M}[T_{0}](\overrightarrow{\phi}), \forall \overrightarrow{\phi} \in \mathbb{U},$$
 (45)

• Weak mechanical problem (WM2): Let $T \in H_r^1(\omega)$ be the solution of the weak thermal model (WT). Under the assumptions (MH1)-(MH3), find $\overrightarrow{u}_T \in \mathbb{U}$ such that,

$$a_{M}(\overrightarrow{u}_{T}, \overrightarrow{\phi}) = l_{M}[T](\overrightarrow{\phi}) - l_{M}[T_{0}](\overrightarrow{\phi}), \ \forall \overrightarrow{\phi} \in \mathbb{U},$$
 (46)

5. Finite element discretization of the thermo-mechanical model

In this section, we are going to briefly describe the Lagrange finite element method used to approximate the problems (WT), and (WM), (WM1) and (WM2).

We introduce the n_h – dimensional space $H^1_{r,h}(\omega) \subset H^1_r(\omega)$ and m_h – dimensional space $\mathbb{U}_h \subset \mathbb{U}$,

$$H_{r,h}^{1}(\omega) = \operatorname{span}\{\psi_{1,h}, \psi_{2,h}, \dots, \psi_{n_{h},h}\},$$
 (47)

$$\mathbb{U}_h = \operatorname{span}\{\overrightarrow{\phi}_{1,h}, \overrightarrow{\phi}_{2,h}, \dots, \overrightarrow{\phi}_{m_h,h}\}. \tag{48}$$

Based on the Galerkin method of weighted residuals [54], we can express the approximated solutions T_h and \overrightarrow{u}_h as follows:

$$T_h = \sum_{i=1}^{n_h} T_h^i \psi_{i,h} , \qquad (49)$$

$$\overrightarrow{u}_h = \sum_{i=1}^{m_h} u_h^i \overrightarrow{\phi}_{i,h} , \qquad (50)$$

where T_h^i and u_h^i are the nodal temperature and nodal displacement, respectively, and the basis functions $\psi_{i,h}$ and $\overrightarrow{\phi}_{i,h}$ are piecewise polynomial of degree $p \ge 1$ in (r, y) space.

Therefore, the approximation of the problem (WT) in the finite dimensional space $H_{r,h}^1$ can be stated as,

• **Problem** $(WT)_h$: Under the assumptions (TH1) - (TH3), find $T_h \in H^1_{r,h}(\omega)$ such that,

$$a_T(T_h, \psi_h) = l_T(\psi_h) , \forall \psi_h \in H^1_{r,h}(\omega) . \tag{51}$$

Similarly, the approximation of the problems (WM), (WM1) and (WM2) in the finite dimensional space \mathbb{U}_h can be stated as:

• **Problem** $(WM)_h$: Let $T_h \in H^1_{r,h}(\omega)$, be the solution of the discretized thermal model $(WT)_h$. Under the assumptions (MH1) - (MH3), find $\overrightarrow{u}_h \in \mathbb{U}_h$ such that,

$$a_M(\overrightarrow{u}_h, \overrightarrow{\phi}_h) = l_M[T_h](\overrightarrow{\phi}_h), \ \forall \overrightarrow{\phi}_h \in \mathbb{U}_h.$$
 (52)

• **Problem** $(WM1)_h$: Under the assumptions (MH1) - (MH3), find $\overrightarrow{u}_{M,h} \in \mathbb{U}_h$ such that,

$$a_{M}(\overrightarrow{u}_{M,h}, \overrightarrow{\phi}_{h}) = l_{M}[T_{0}](\overrightarrow{\phi}_{h}), \ \forall \overrightarrow{\phi}_{h} \in \mathbb{U}_{h}.$$
 (53)

• **Problem** $(WM2)_h$: Let $T_h \in H^1_{r,h}(\omega)$, be the solution of the discretized thermal model $(WT)_h$. Under the assumptions (MH1) - (MH3), find $\overrightarrow{u}_{T,h} \in \mathbb{U}_h$ such that,

$$a_{M}(\overrightarrow{u}_{T,h},\overrightarrow{\phi}_{h}) = l_{M}[T_{h}](\overrightarrow{\phi}_{h}) - l_{M}[T_{0}](\overrightarrow{\phi}_{h}), \ \forall \overrightarrow{\phi}_{h} \in \mathbb{U}_{h}.$$
 (54)

6. Validation of the full order model

In this section we verify the numerical implementation of the FOM introduced in Secs. 4 and 5. In Sec. 6.1, we report details about the construction of the computational grid used for numerical simulations. Then proper benchmark tests for $(WT)_h$, $(WM)_h$, $(WM1)_h$ and $(WM2)_h$ problems are investigated in Sec. 6.2. All the FOM computations have been performed by using the python finite element library FEniCS [1].

r	0	7.05	7.05	5.30	5.30	4.95	4.95	4.6	4.6	4.25	4.25	0
У	0	0	7.265	7.265	4.065	4.065	3.565	3.565	2.965	2.965	2.365	2.365

Table 1: coordinates (in m) of the vertices of domain ω (see Figure 3).

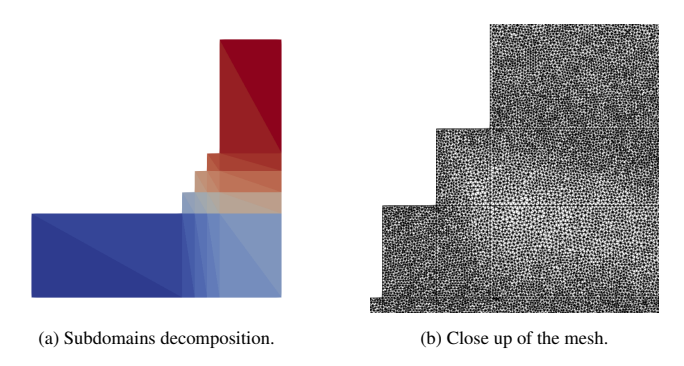


Figure 4: Discretization of the domain ω .

6.1. Computational domain and mesh

The coordinates of the 12 vertices constituting the domain illustrated in Figure 3 are reported in Table 1.

Since one of the main objectives of this work is to develop MOR able to work in a geometrical parametrization setting, before proceeding to the meshing, we consider a decomposition of the domain into n_{su} triangular subdomains as (see, e.g., [29, 43]),

$$\omega = \bigcup_{i=1}^{n_{su}} \omega_i , \ \omega_i \cap \omega_j = \emptyset \text{ for } i \neq j , \ 1 \leq i, j \leq n_{su} . \tag{55}$$

We set $n_{su} = 30$ (see Figure 4a). The considered mesh is compliant with the triangular subdomains and contains 121137 triangular elements and 61147 vertices (see Figure 4b). The minimum and maximum mesh size, that is measured as distance between vertices of an element of the mesh, are 0.011m and 0.045m respectively. The quality of each mesh element, q_e , could be estimated by using the following formula [50]:

$$q_e = \frac{4\sqrt{3}A}{l_1^2 + l_2^2 + l_3^2} \,,$$
(56)

where A is the area of the element, and l_1 , l_2 and l_3 are the lengths of its three edges. The minimum value of q_e was 0.25, that is sufficiently far from zero.

6.2. Benchmark tests

The pipeline that we follow for the design of reliable benchmark tests to be used for the FOM validation consists of three steps:

- We set analytical expressions for temperature and displacement.
- We calculate corresponding model data, including boundary conditions and source terms, in order to identify the FOM for which the analytical relationships are solutions.
- Finally, we numerically solve the problem and compare the computational solutions with the analytical ones.

We consider the physical properties reported in Table 2 for all numerical simulations shown in this section.

6.2.1. Thermal model

We consider the following analytical expression for the temperature,

$$T_a(r, y) = C'r^2y$$
, with $C' = 1K/m^3$. (57)

Then:

Property	Value
Thermal conductivity k	$10\frac{W}{mK}$
Convection coefficient $h_{c,-}$	$2000 \frac{W}{m^2 K}$
Convection coefficient $h_{c,f}$	$200 \frac{W}{m^2 K}$
Convection coefficient $h_{c,out}$	$2000 \frac{W}{m^2 K}$
Young's modulus E	5e9Pa
Poisson's ratio v	0.2
Thermal expansion coefficient α	$10^{-6}/K$
Reference temperature T_0	298 <i>K</i>
Gravitational acceleration g	$9.81 \frac{m}{s^2}$

Table 2: Physical properties values used for the FOM benchmark tests.

• the corresponding source term Q is obtained by using eq. (23),

$$Q(r,y) = -k\frac{\partial^2 T_a}{\partial r^2} - k\frac{\partial^2 T_a}{\partial y^2} - \frac{k}{r}\frac{\partial T_a}{\partial r} = -4C'ky,$$
(58)

• the heat flux q_+ , as well as the temperatures T_f , T_{out} and T_- , are derived from eq. (24),

on
$$\gamma_+: q_+(r, y) = -k\frac{\partial T_a}{\partial y} = -C'kr^2$$
, (59a)

on
$$\gamma_{sf}$$
: $T_f = T_a + \frac{k}{h_{c,f}} \left(\frac{\partial T_a}{\partial r} n_r + \frac{\partial T_a}{\partial y} n_y \right)$

$$=C'r^2y+C'\frac{k}{h_{c,f}}(2ryn_r+r^2n_y)\;, (59b)$$

on
$$\gamma_{out}$$
: $T_{out} = T_a + \frac{k}{h_{c,out}} \frac{\partial T_a}{\partial r} = C'r^2y + C' \frac{2ryk}{h_{c,out}}$, (59c)

on
$$\gamma_{-}: T_{-} = T_{a} - \frac{k}{h_{c-}} \frac{\partial T_{a}}{\partial y} = C' r^{2} y - C' \frac{r^{2} k}{h_{c-}},$$
 (59d)

and it is verified that

on
$$\gamma_s$$
: $\frac{\partial T_a}{\partial r} = 0$. (60a)

We solve the $(WT)_h$ problem for the data Q, q_+ , T_f , T_{out} , T_- given by equations (58)-(60a). We choose a discretized space of polynomial of degree 3. Analytical and numerical solutions are reported in Figure 5 (left and center). As we can see, a very good agreement is obtained. For a more quantitative comparison, we also display the absolute error in Figure 5 (right), and compute the relative error,

$$\frac{||T_a - T_h||_{H_r^1(\omega)}}{||T_a||_{H_r^1(\omega)}} = 7e - 13.$$

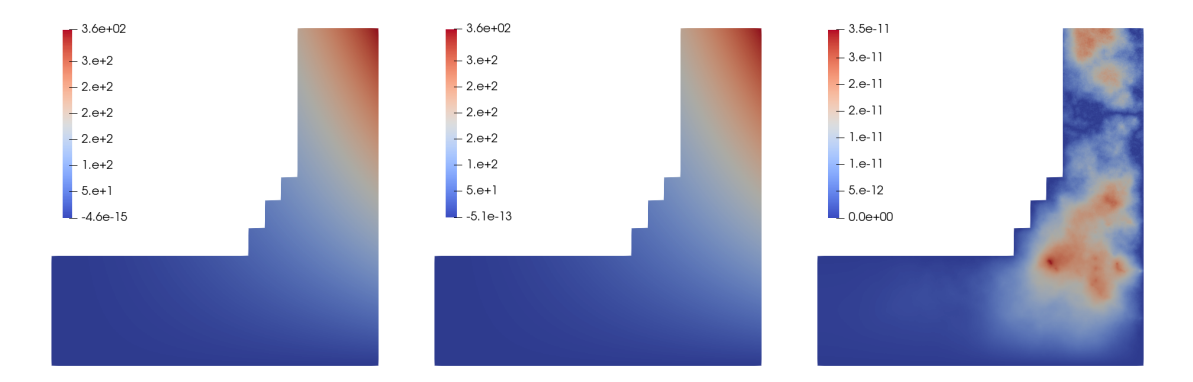


Figure 5: Benchmark for the thermal model $(WT)_h$: analytical temperature T_a (left), numerical temperature T_h (center), and corresponding absolute error $|T_a - T_h|$ (right) in K.

6.2.2. Mechanical model

Firstly, we consider that the body is at reference temperature $T = T_0$, i.e. thermal stresses $(2\mu + 3\lambda)\alpha(T - T_0)$ are not present. Therefore, we refer to the problem $(WM1)_h$.

We consider a known displacement function

$$\vec{u}_a = C(ry^2, r^2y), \text{ with } C = 1e - 4/m^2.$$
 (61)

Then:

• the components of the stress tensor σ are given by eqs. (22) as,

$$\sigma_{rr} = \frac{E}{(1 - 2\nu)(1 + \nu)} (Cy^2 + \nu Cr^2) , \qquad (62a)$$

$$\sigma_{yy} = \frac{E}{(1 - 2\nu)(1 + \nu)} (2\nu Cy^2 + (1 - \nu)Cr^2), \qquad (62b)$$

$$\sigma_{\theta\theta} = \frac{E}{(1 - 2\nu)(1 + \nu)} (Cy^2 + \nu Cr^2) , \qquad (62c)$$

$$\sigma_{ry} = \frac{2ECry}{(1+y)} \,. \tag{62d}$$

• the source term $\overrightarrow{f}_0 = [f_{0,r} \ f_{0,y}]$ is obtained from eqs. (25) and (62) as,

$$f_{0,r} = -\left(\frac{\partial \sigma_{rr}}{\partial r} + \frac{\partial \sigma_{ry}}{\partial y} + \frac{\sigma_{rr} - \sigma_{\theta\theta}}{r}\right)$$
$$= -\left(\frac{2E\nu Cr}{(1 - 2\nu)(1 + \nu)} + \frac{2ECr}{(1 + \nu)}\right), \tag{63a}$$

$$f_{0,y} = -\left(\frac{\partial \sigma_{ry}}{\partial r} + \frac{\partial \sigma_{yy}}{\partial y} + \frac{\sigma_{ry}}{r}\right)$$

$$= -\left(\frac{4ECy}{(1+v)} + \frac{4EvCy}{(1-2v)(1+v)}\right). \tag{63b}$$

• the boundary tractions are derived from eqs. (26) and (62) as,

on
$$\gamma_{+}$$
: $g_{+,r} = \frac{2ECry}{(1+\nu)}$, (64a)

$$g_{+,y} = \frac{E}{(1 - 2\nu)(1 + \nu)} \left(2\nu C y^2 + (1 - \nu)C r^2 \right) , \tag{64b}$$

on
$$\gamma_{-}$$
: $g_{-,r} = -\frac{2ECry}{(1+v)}$, (64c)

on
$$\gamma_{sf}$$
: $g_{sf,r} = \frac{E}{(1 - 2\nu)(1 + \nu)} \left(Cy^2 + \nu Cr^2 \right) n_r + \frac{2ECry}{(1 + \nu)} n_y$, (64d)

$$g_{sf,y} = \frac{2ECry}{(1+\nu)}n_r + \frac{E}{(1-2\nu)(1+\nu)} \left(2\nu Cy^2 + (1-\nu)Cr^2\right)n_y,$$
 (64e)

on
$$\gamma_{out}$$
: $g_{out,r} = \frac{E}{(1-2\nu)(1+\nu)} \left(Cy^2 + \nu Cr^2\right)$, (64f)

$$g_{out,y} = \frac{2ECry}{(1+v)},$$
 (64g)

and it is verified that

on
$$\gamma_- \cup \gamma_s : \overrightarrow{u}_a \cdot \overrightarrow{n} = 0$$
. (65a)

We solve the $(WM1)_h$ problem for the data given by equations (63a) - (65a) by using a discretized space of polynomial of degree 3. The magnitude of the analytical and numerical displacement, as well as the associated absolute error, are represented in Figure 6. Moreover, we compute the relative error

$$\frac{|\overrightarrow{u}_a - \overrightarrow{u}_h||_{\mathbb{U}}}{|\overrightarrow{u}_a||_{\mathbb{U}}} = 1.81e - 12.$$

Like the thermal model, even in this case we could observe that the two solutions show a very good agreement. For further comparison, we also computed the Von Mises stress:

$$\sigma_{vm} = \sqrt{\frac{3}{2}\sigma_d : \sigma_d} \,, \tag{66}$$

where σ_d is the deviatoric part of the stress tensor

$$\sigma_d = \sigma - \frac{1}{3} Tr(\sigma) \boldsymbol{I} . \tag{67}$$

We display the magnitude of the analytical and numerical Von Mises stress, σ_{vma} and σ_{vmh} respectively, and the corresponding absolute error in Figure 7. We see that a very good matching is obtained.

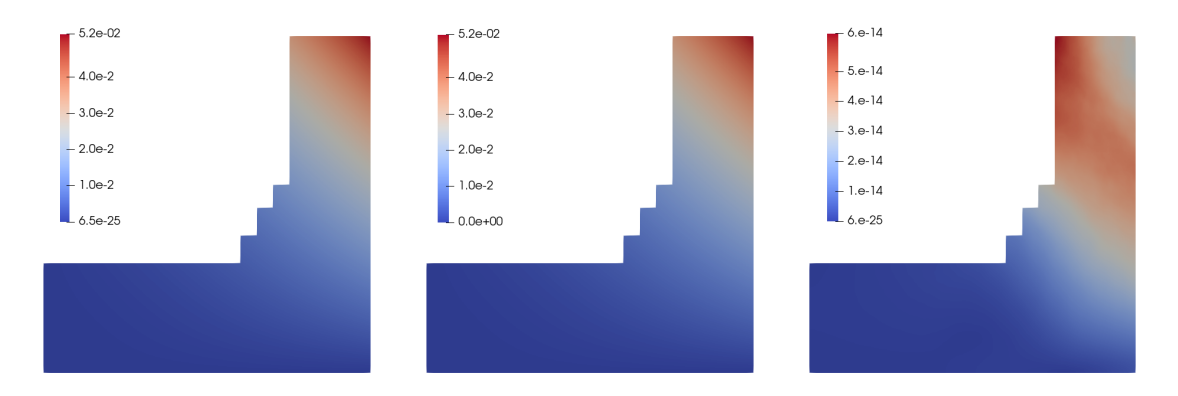


Figure 6: Benchmark for the mechanical model $(WM1)_h$: analytical displacement magnitude $|\overrightarrow{u}_a|$ (left), numerical displacement magnitude $|\overrightarrow{u}_h|$ (center), and absolute error magnitude $|\overrightarrow{u}_a - \overrightarrow{u}_h|$ (right) in m.

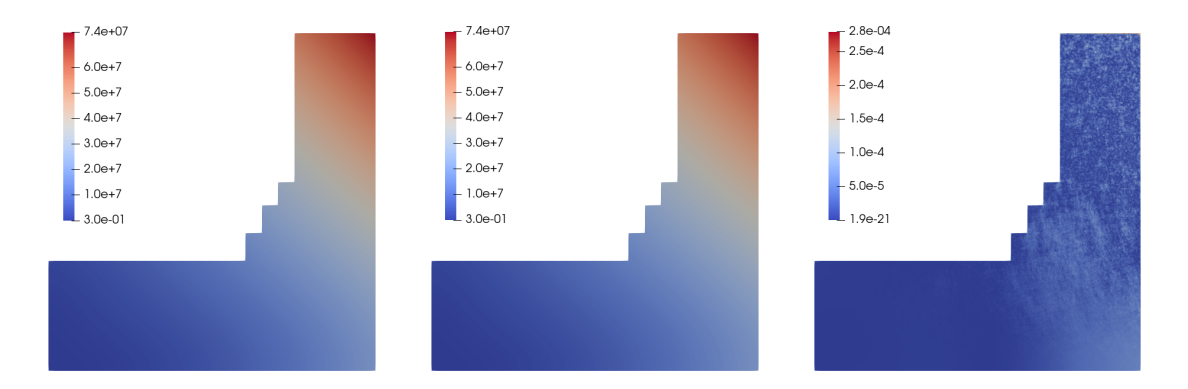


Figure 7: Benchmark for the mechanical model $(WM1)_h$: analytical Von Mises stress magnitude σ_{vma} (left), numerical Von Mises stress magnitude σ_{vmh} (center), and absolute error $|\sigma_{vmh} - \sigma_{vma}|$ (right) in N/m².

Now we address the coupling between the thermal and mechanical effects, so we refer to the problem $(WM)_h$. We assume for the temperature the analytical field used for the problem $(WT)_h$, T_a (see eq. (57)), and for the displacement the analytical field used for the problem $(WM1)_h$, \overrightarrow{u}_a (see eq. (61)). Then:

• we obtain the thermal stresses from eqs. (4) and (6):

$$(2\mu + 3\lambda)\alpha(T - T_0) = (2\mu + 3\lambda)\alpha(C'r^2y - T_0) = \frac{E}{(1 - 2\nu)}\alpha(C'r^2y - T_0).$$

• the components of the stress tensor σ are given by eqs. (22):

$$\sigma_{rr} = \frac{E}{(1 - 2\nu)(1 + \nu)} (Cy^2 + \nu Cr^2) - \frac{E}{(1 - 2\nu)} \alpha (C'r^2y - T_0) , \qquad (68a)$$

$$\sigma_{yy} = \frac{E}{(1 - 2\nu)(1 + \nu)} (2\nu C y^2 + (1 - \nu)C r^2) - \frac{E}{(1 - 2\nu)} \alpha (C' r^2 y - T_0), \qquad (68b)$$

$$\sigma_{\theta\theta} = \frac{E}{(1 - 2\nu)(1 + \nu)} (Cy^2 + \nu Cr^2) - \frac{E}{(1 - 2\nu)} \alpha (C'r^2y - T_0) , \qquad (68c)$$

$$\sigma_{ry} = \frac{2ECry}{(1+y)} \,. \tag{68d}$$

• the source term $\overrightarrow{f}_0 = [f_{0,r} \ f_{0,y}]$ is obtained from eqs. (25) and (62) by:

$$f_{0,r} = -\left(\frac{\partial \sigma_{rr}}{\partial r} + \frac{\partial \sigma_{ry}}{\partial y} + \frac{\sigma_{rr} - \sigma_{\theta\theta}}{r}\right)$$

$$= -\left(\frac{2E\nu Cr}{(1 - 2\nu)(1 + \nu)} + \frac{2ECr}{(1 + \nu)} - \frac{2C'ryE\alpha}{(1 - 2\nu)}\right),$$
(69a)

$$f_{0,y} = -\left(\frac{\partial \sigma_{ry}}{\partial r} + \frac{\partial \sigma_{yy}}{\partial y} + \frac{\sigma_{ry}}{r}\right)$$

$$= -\left(\frac{4ECy}{(1+v)} + \frac{4EvCy}{(1-2v)(1+v)} - \frac{C'r^2E\alpha}{(1-2v)}\right). \tag{69b}$$

• the boundary tractions are derived from eqs. (26) and (62) as:

on
$$\gamma_{+}: g_{+,r} = \frac{2ECry}{(1+\nu)}$$
, (70a)

$$g_{+,y} = \frac{E}{(1 - 2\nu)(1 + \nu)} \left(2\nu C y^2 + (1 - \nu)C r^2 \right)$$

$$-\frac{E\alpha}{(1-2\nu)}(C'r^2y - T_0),$$
 (70b)

on
$$\gamma_{-}: g_{-,r} = -\frac{2ECry}{(1+v)}$$
, (70c)

on
$$\gamma_{sf}$$
: $g_{sf,r} = \frac{E}{(1-2\nu)(1+\nu)}(Cy^2 + \nu Cr^2)n_r$

$$-\frac{E\alpha}{(1-2\nu)}(C'r^2y - T_0)n_r + \frac{2ECry}{(1+\nu)}n_y,$$
(70d)

$$g_{sf,y} = \frac{E}{(1 - 2\nu)(1 + \nu)} \left(2\nu C y^2 + (1 - \nu)Cr^2 \right) n_y$$

$$-\frac{E\alpha}{(1-2\nu)}(C'r^2y - T_0)n_y + \frac{2ECry}{(1+\nu)}n_r , \qquad (70e)$$

on
$$\gamma_{out}$$
: $g_{out,r} = \frac{E}{(1-2\nu)(1+\nu)}(Cy^2 + \nu Cr^2) - \frac{E\alpha}{(1-2\nu)}(C'r^2y - T_0)$, (70f)

$$g_{out,y} = \frac{2ECry}{(1+v)} \,. \tag{70g}$$

We display the magnitude of the analytical displacement and Von Mises stress comparing them with the corresponding numerical values in Figures 8 and 9, respectively, and compute the relative error

$$\frac{||\overrightarrow{u}_a - \overrightarrow{u}_h||_{\mathbb{U}}}{||\overrightarrow{u}_a||_{\mathbb{U}}} = 2.2e - 12.$$

We could see that, as for mechanical model $(WM1)_h$, the agreement between the two solutions is very good.

Finally, we observe that the difference between the hydrostatic stress computed with the model $(WM)_h$ and the one computed with the model $(WM1)_h$, i.e. the hydrostatic stress related to the model $(WM2)_h$, should be equal to the thermal stress:

$$\frac{1}{3}tr\left(\boldsymbol{\sigma}(\overrightarrow{u_h})[T_h] - \boldsymbol{\sigma}(\overrightarrow{u_h})[T_0]\right) = (2\mu + 3\lambda)\alpha(T_h - T_0)\boldsymbol{I}.$$
(71)

The right and hand sides of eq. (71) are shown in Figure 10. We obtain a very good agreement.

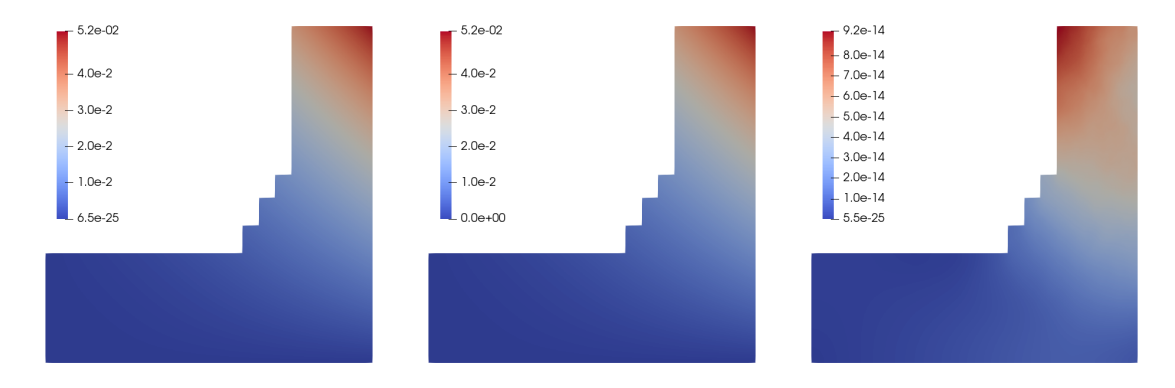


Figure 8: Benchmark for the mechanical problem $(WM)_h$: analytical displacement magnitude $|\vec{u}_a|$ (left), numerical displacement magnitude $|\vec{u}_h|$ (center), and absolute error $|\vec{u}_a - \vec{u}_h|$ (right) in m.

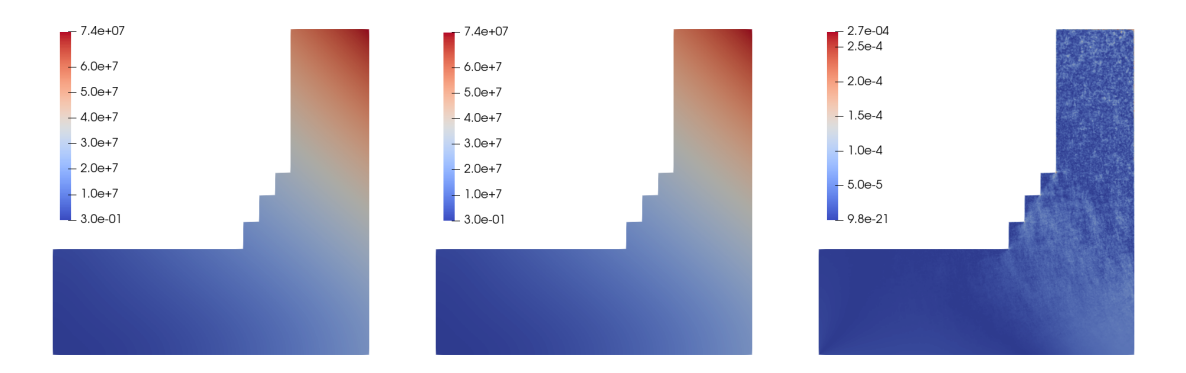


Figure 9: Benchmark for the mechanical problem $(WM)_h$: analytical Von Mises stress σ_{vma} (left), numerical Von Mises stress σ_{vmh} (center) and absolute error $|\sigma_{vmh} - \sigma_{vma}|$ (right) in N/m².

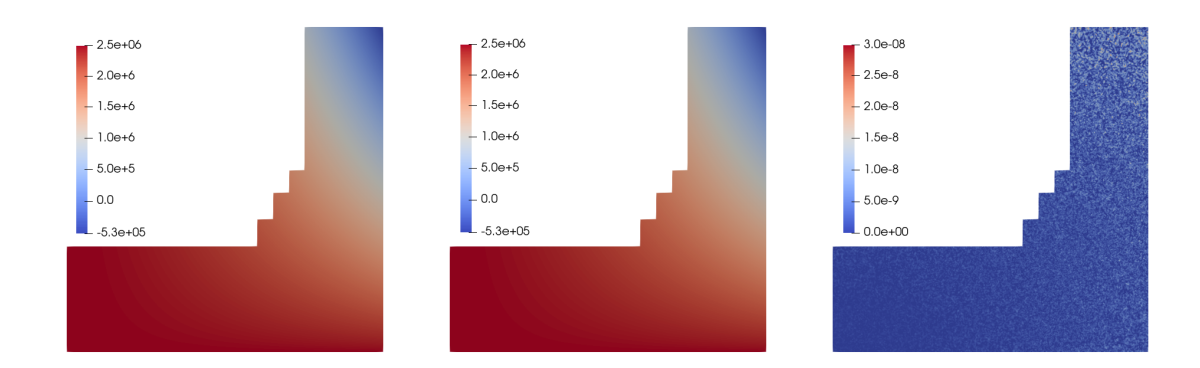


Figure 10: Benchmark for the mechanical model $(WM2)_h$: difference between the hydrostatic stress computed with the $(WM)_h$ model and the $(WM1)_h$ model $\frac{1}{3}tr\left(\sigma(\overrightarrow{u_h})[T_h] - \sigma(\overrightarrow{u_h})[T_0]\right)$ (left), thermal stress $(2\mu + 3\lambda)\alpha(T_h - T_0)$ (center) and corresponding absolute error $\left|\frac{1}{3}tr\left(\sigma(\overrightarrow{u_h})[T_h] - \sigma(\overrightarrow{u_h})[T_0]\right) - (2\mu + 3\lambda)\alpha(T_h - T_0)\right|$ (right) in N/m².

7. Model order reduction

In this section, we present our MOR framework. Firstly, we introduce the parameter space related to the problem under investigation (Sec. 7.1). Then, in Sec. 7.2, we describe the POD algorithm that is used for the construction of reduced basis space as well as the two methods adopted for the computation of the reduced degrees of freedom, Galerkin projection (G) and Artificial Neural Network (ANN). Finally, in Sec. 7.3, we show some numerical tests with the aim to validate our approach. The MOR computations have been carried out using RBniCS [25, 41], an in-house open source python library employing several reduced order techniques based on FEniCS [1, 16], and PyTorch [35, 37], a python machine learning library.

7.1. Parameter space

Let $\mathbb{P} \subset \mathbb{R}^d$ be the parameter space having dimensionality d with $\Xi \in \mathbb{P}$ a tuple of parameters. For the problem of the hearth blast furnace, the relevant parameters are related both to the physical properties and the geometry of the domain ω . The physical parameters are the thermal conductivity of the material, k, the thermal expansion coefficient, α , the Young modulus, E, and the Poisson's ratio, ν . On the other hand, the geometric parameters are the diameter of each section of the hearth D_0, D_1, D_2, D_3, D_4 , and the thickness of each section of the hearth t_0, t_1, t_2, t_3, t_4 (see Figure 11). So for the problem under consideration, in the most general case (i.e., when all the parameters are considered), we have $\Xi = \{\Xi_p, \Xi_g\}$ where $\Xi_p = \{k, \alpha, E, \nu\} \in \mathbb{P}_p \subset \mathbb{R}^4$ is the physical parameters tuple and $\Xi_g = \{D_0, D_1, D_2, D_3, D_4, t_0, t_1, t_2, t_3, t_4\} \in \mathbb{P}_g \subset \mathbb{R}^{10}$ is the geometric parameters tuple, and d = 14.

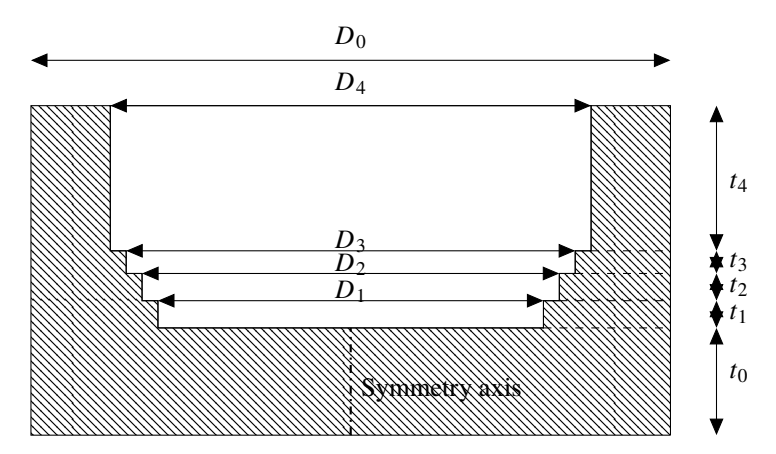


Figure 11: Hearth geometric parameters.

Let us consider a geometrical parameters tuple $\bar{\Xi}_g$ and the corresponding domain $\hat{\omega} = \omega(\bar{\Xi}_g)$. We refer to $\hat{\omega}$ as the reference domain. As discussed in Sec. 6.1, the domain $\hat{\omega}$ is divided into n_{su} non-overlapping triangular subdomains i.e. $\hat{\omega} = \bigcup_{i=1}^{n_{su}} \hat{\omega}_i$, $\hat{\omega}_i \cap \hat{\omega}_j = \emptyset$, $i \neq j$. For each of the subdomains $\hat{\omega}_i$, one can consider an invertible mapping F_i ,

$$F_i: \hat{\omega}_i \times \mathbb{P}_g \to \omega_i ,$$
 (72)

of the form

$$\overrightarrow{x} = F_i(\overrightarrow{x}, \Xi_g) = G_{F,i}(\Xi_g)\overrightarrow{x} + \overrightarrow{c}_{F,i}(\Xi_g); , \forall \overrightarrow{x} \in \hat{\omega}_i, \forall \overrightarrow{x} \in \omega_i(\Xi_g),$$
(73)

where

$$\mathbf{G}_{F,i} = \begin{bmatrix} G_{F,i,11} & G_{F,i,12} \\ G_{F,i,21} & G_{F,i,22} \end{bmatrix}, \ \overrightarrow{x} = \{r \ y\}^T, \ \overrightarrow{\hat{x}} = \{\hat{r} \ \hat{y}\}^T, \ \overrightarrow{c}_{F,i} = \{c_{F,i,1} \ c_{F,i,2}\}^T.$$
 (74)

Equation (73) highlights that the Jacobian matrix $G_{F,i}$ and translation vector $\overrightarrow{c}_{F,i}$ are dependent only on the geometric parameters tuple Ξ_g and do not vary over a given subdomain. In the following, the domains ω will be the image by eq. (73) of the reference domain for the tuples of geometric parameters considered.

7.2. Main ingredients of MOR

The basic idea of MOR is the assumption that solutions live in a low dimensional manifold. Thus, any solution can be approximated based on a reduced number of global basis functions.

We seek the reduced basis approximations $T_h^{rb} \in H_{r,h}^{1,rb}(\omega)$ and $\overrightarrow{u}_h^{rb} \in \mathbb{U}_h^{rb}$ of $T_h \in H_{r,h}^1(\omega)$ and $\overrightarrow{u}_h \in \mathbb{U}_h$, respectively. The reduced basis spaces $H_{r,h}^{1,rb}(\omega) \subset H_{r,h}^1(\omega)$ and $\mathbb{U}_h^{rb} \subset \mathbb{U}_h$ are given by,

$$\begin{split} H_{r,h}^{1,rb}(\omega) &= \operatorname{span}\{\psi_h^1,\dots,\psi_h^{N_T}\}\;,\\ \mathbb{U}_h^{rb} &= \operatorname{span}\{\overrightarrow{\phi}_h^1,\dots,\overrightarrow{\phi}_h^{N_M}\}\;, \end{split}$$

where $N_M \ll m_h$ and $N_T \ll m_h$ are the number of basis functions forming the reduced basis spaces $H_{r,h}^{1,rb}(\omega)$ and \mathbb{U}_h^{rb} , respectively. Then we can represent $\overrightarrow{u}_h^{rb}$ and T_h^{rb} by

$$T_h^{rb} = \sum_{i=1}^{N_T} \zeta_T^i \psi_h^i \,, \tag{75}$$

$$\overrightarrow{u}_{h}^{rb} = \sum_{i=1}^{N_{M}} \zeta_{M}^{i} \overrightarrow{\phi}_{h}^{i} , \qquad (76)$$

where $\{\zeta_T^i\}_{i=1}^{N_T}$ and $\{\zeta_M^i\}_{i=1}^{N_M}$ are the temperature and displacement degrees of freedom, respectively.

We also construct the reduced basis spaces for displacement fields \overrightarrow{u}_T and \overrightarrow{u}_M , introduced in (53) and (54), as,

$$\begin{split} \mathbb{U}^{rb}_{T,h} &= \operatorname{span}\{\overrightarrow{\phi}_{T,h}^{1}, \ldots, \overrightarrow{\phi}_{T,h}^{N_{M,T}}\}\;,\\ \mathbb{U}^{rb}_{M,h} &= \operatorname{span}\{\overrightarrow{\phi}_{M,h}^{1}, \ldots, \overrightarrow{\phi}_{M,h}^{N_{M,M}}\}\;. \end{split}$$

So, the reduced basis approximations $\overrightarrow{u}_{M,h}^{rb} \in \mathbb{U}_{M,h}^{rb}$ of $\overrightarrow{u}_{M,h} \in \mathbb{U}_h$ and $\overrightarrow{u}_{T,h}^{rb} \in \mathbb{U}_{T,h}^{rb}$ of $\overrightarrow{u}_{T,h} \in \mathbb{U}_h$ can be represented as,

$$\overrightarrow{u}_{M,h}^{rb} = \sum_{i=1}^{N_{M,M}} \zeta_{M,M}^{i} \overrightarrow{\phi}_{M,h}^{i}, \overrightarrow{u}_{T,h}^{rb} = \sum_{i=1}^{N_{M,T}} \zeta_{M,T}^{i} \overrightarrow{\phi}_{T,h}^{i}. \tag{77}$$

7.2.1. POD algorithm

In the literature, one can find several techniques to generate the reduced basis spaces, e.g. Proper Orthogonal Decomposition (POD), the Proper Generalized Decomposition (PGD) and the Reduced Basis (RB) with a greedy sampling strategy. See, e.g., [3, 8, 21, 25, 38]. In this work, the reduced basis spaces are constructed by POD that is able to capture the "dominant" modes by exploiting the information contained in the full order snapshots.

We are going to describe the procedure for the computation of the reduced basis space $H_{r,h}^{1,rb}(\omega)$. The reduced basis space \mathbb{U}_h^{rb} , $\mathbb{U}_{T,h}^{rb}$ and $\mathbb{U}_{M,h}^{rb}$ are constructed in an analogous way. First, n_s parameter tuples, $\{\Xi_k\}_{k=1}^{n_s}$, are considered that form the training set. We compute the snapshots $T_h(\Xi_k)$ related to each parameter tuple in the training set. Then a matrix $C_T \in \mathbb{R}^{n_s \times n_s}$ is constructed,

$$(C_T)_{kl} = \langle T_h(\Xi_k), T_h(\Xi_l) \rangle_{H^1_{r,h}(\hat{\omega})}, \ 1 \le k, l \le n_s,$$
 (78)

where transformation (73) is considered. Next, N_T largest eigenvalues $\{\theta_T^i\}_{i=1}^{N_T}$ of the matrix C_T , sorted in descending order, $\theta_T^1 \geq \theta_T^2 \geq \ldots \geq \theta_T^{N_T}$, and corresponding eigenvectors $\{V_T^i\}_{i=1}^{N_T}, V_T^i \in \mathbb{R}^{n_s}$, are computed,

$$C_T V_T^i = \theta_T^i V_T^i \ . \tag{79}$$

The reduced basis are then given by

$$\psi_h^i = \frac{\sum_{k=1}^{n_s} (V_T^i)_k T_h(\Xi_k)}{||\sum_{k=1}^{n_s} (V_T^i)_k T_h(\Xi_k)||_{H_{r,h}^1(\hat{\omega})}}, \ 1 \le i \le N_T.$$
(80)

In order to determine the admissibility of a given eigenvector into the POD space, we refer to the following criterion

$$\frac{\theta_T^i}{\theta_T^1} \ge 1e - 4. \tag{81}$$

In the following subsections, we describe two different approaches for the computation of the degrees of freedom: Galerkin projection (G) and Artificial Neural Network (ANN).

7.2.2. Galerkin projection

Here we choose to consider $(WM1)_h$ and $(WM2)_h$ in the place of $(WM)_h$ because each subsystem may have different scale effects: see, e.g., [28, 46, 53]. We consider an affine parametric dependence, i.e. the bilinear forms $a_T(\cdot,\cdot;\Xi)$ and $a_M(\cdot,\cdot;\Xi)$ are expressed as weighted sum of n_{a_T} and n_{a_M} parameter independent bilinear forms. Similarly, the linear forms $l_T(\cdot;\Xi)$ and $l_M[T](\cdot;\Xi)$ are expressed as weighted sum of n_{l_T} and n_{l_M} parameter independent linear forms. We have:

$$a_{T}(T, \psi; \Xi) = \sum_{i=1}^{n_{a_{T}}} \theta_{a_{T,i}}(\Xi) a_{T,i}(T, \psi; \bar{\Xi}) ,$$

$$l_{T}(\psi; \Xi) = \sum_{i=1}^{n_{l_{T}}} \theta_{l_{T,i}}(\Xi) l_{T,i}(\psi; \bar{\Xi}) ,$$
(82)

and

$$a_{M}(\overrightarrow{u}, \overrightarrow{\phi}; \Xi) = \sum_{i=1}^{n_{a_{M}}} \theta_{a_{M,i}}(\Xi) a_{M,i}(\overrightarrow{u}, \overrightarrow{\phi}; \overline{\Xi}) ,$$

$$l_{M}[T](\overrightarrow{\phi}; \Xi) = \sum_{i=1}^{n_{l_{M}}} \theta_{l_{M,i}}(\Xi) l_{M,i}[T](\overrightarrow{\phi}; \overline{\Xi}) .$$
(83)

The affine expansion of operators is essentially a change of variables and has been widely addressed in the literature: see, e.g., [8, 21, 25]. The affinity assumption is particularly important as it leads to considerable efficiency. This is mainly due to the fact that the evaluation of bilinear forms, $a_{M,i}(\overrightarrow{u}, \overrightarrow{\phi})$ and $a_{T,i}(T, \psi)$, and linear forms, $l_{T,i}(\psi)$ and $l_{M,i}[T](\overrightarrow{\phi})$ are not required for each new tuple of parameters.

So for what concerns the model $(WT)_h$, the bilinear form $a_{T,h}:H^1_{r,h}(\omega)\times H^1_{r,h}(\omega)\to\mathbb{R}$ is restricted to the reduced basis space as $a^{rb}_{T,h}:H^{1,rb}_{r,h}(\omega)\times H^{1,rb}_{r,h}(\omega)\to\mathbb{R}$. In the same way, the linear form $l_{T,h}:H^1_{r,h}(\omega)\to\mathbb{R}$ is restricted to the reduced basis space as $l^{rb}_{T,h}:H^{1,rb}_{r,h}(\omega)\to\mathbb{R}$. So the reduced basis approximation T^{rb}_h at a given parameter tuple Ξ^* is obtained by solving

$$a_{T,h}^{rb}(T_h^{rb}, \psi_h^{rb}; \Xi^*) = l_{T,h}^{rb}(\psi_h^{rb}; \Xi^*), \ \forall \psi_h^{rb} \in H_{r,h}^{1,rb}(\omega).$$
 (84)

On the other hand, for what concerns the model $(WM1)_h$, the bilinear form $a_{M,h}: \mathbb{U}_h \times \mathbb{U}_h \to \mathbb{R}$ is restricted to the reduced basis space as $a_{M,h}^{rb}: \mathbb{U}_{M,h}^{rb} \times \mathbb{U}_{M,h}^{rb} \to \mathbb{R}$. The linear form $l_{M,h}: \mathbb{U}_h \to \mathbb{R}$ is restricted to the reduced basis space as $l_{M,h}^{rb}: \mathbb{U}_{M,h}^{rb} \to \mathbb{R}$. So the reduced basis approximation $\overrightarrow{u}_{M,h}^{rb}$ at a given parameter tuple Ξ^* is obtained by solving,

$$a_{M,h}^{rb}(\overrightarrow{u}_{M,h}^{rb},\overrightarrow{\phi}_{M,h}^{rb};\Xi^*) = l_{M,h}^{rb}[T_0](\overrightarrow{\phi}_{M,h}^{rb};\Xi^*), \ \forall \overrightarrow{\phi}_{M,h}^{rb} \in \mathbb{U}_{M,h}^{rb}. \tag{85}$$

Similarly, for the model $(WM2)_h$ the bilinear form $a_{M,h}: \mathbb{U}_h \times \mathbb{U}_h \to \mathbb{R}$ is restricted to the reduced basis space as $a_{M,h}^{rb}: \mathbb{U}_{T,h}^{rb} \times \mathbb{U}_{T,h}^{rb} \to \mathbb{R}$. The linear form $l_{M,h}: \mathbb{U}_h \to \mathbb{R}$ is restricted to the reduced basis space as $l_{M,h}^{rb}: \mathbb{U}_{T,h}^{rb} \to \mathbb{R}$. So, the reduced basis approximation $\overrightarrow{u}_{T,h}^{rb}$ at a given parameter Ξ^* is obtained by solving,

$$a_{Mh}^{rb}(\overrightarrow{u}_{Th}^{rb},\overrightarrow{\phi}_{Th}^{rb};\Xi^*) = l_{Mh}^{rb}[T_h^{rb}](\overrightarrow{\phi}_{Th}^{rb};\Xi^*) - l_{Mh}^{rb}[T_0](\overrightarrow{\phi}_{Th}^{rb};\Xi^*), \ \forall \overrightarrow{\phi}_{Th}^{rb} \in \mathbb{U}_{Th}^{rb}. \tag{86}$$

7.2.3. Artificial Neural Network

Artificial Neural Network (ANN) is a computational model that takes inspiration from the human brain consisting of an interconnected network of simple processing units that can learn from experience by modifying their connections (see, e.g., [22, 42]).

Recently, the application of deep learning methods to partial differential equations has shown promising capabilities: see, e.g., [32, 33, 39, 13, 40, 47]. Concerning the application of the ANN approach in a MOR context, the reader is referred, e.g., to [24, 44, 49, 13, 36, 51]. We highlight that, unlike the Galerkin projection, ANN is a data-driven approach, i.e. based only on data and does not require the knowledge of the original equations describing the system. It is also non-intrusive, in the sense that no modification of the simulation software is required.

In this work, we use a feed-forward ANN consisting of input layer, hidden layers, and output layer, with n_l the total number of layers and d_l the number of unit cells (the so-called neurons) of the l-th layer. The neurons of each layer are connected to the neurons of the next layer by synapses. See Figure 12 for an illustrative representation of a feed-forward ANN.

Each neuron of the l-th layer takes a set of inputs s_i^l from the (l-1)-th layer provided by [15]:

$$s_i^l = \sum_{j=1}^{d_{(l-1)}} w_{ij}^l h_j^{(l-1)} , i = 1, \dots, d_l ,$$
 (87)

where $w_{ij}^{(l)}$ are weights linking the (l-1)-th and l-th layers. Then the output of the l-th layer is given by

$$h_i^{(l)} = f_a \left(s_i^l + b_i^l \right), \ i = 1, \dots, d_l,$$
 (88)

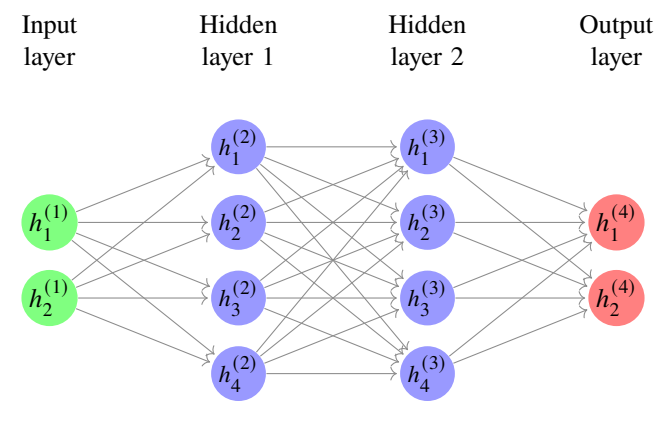


Figure 12: Sketch of a feed-forward ANN with $n_I = 4$.

where $b_i^{(l)}$ are the biasing parameters of the layer l. The weights $w_{ij}^{(l)}$ as well as the biasing parameters $b_i^{(l)}$ are iteratively adjusted by the backpropagation process using an optimization algorithm [30]. The function f_a is a nonlinear differentiable function, called activation function [52]. In this work, we consider for hidden layers the Sigmoid activation function that can be expressed as:

$$f_a(x) = \frac{1}{1 + e^{-x}} \,, \tag{89}$$

whilst for the initial and final layer we use the identity function.

Unlike what done for the Galerkin projection approach, concerning the mechanical problem, we consider the model $(WM)_h$. This choice is due to the fact that ANN suffers from high offline cost because of the training phase, so it is beneficial to train one only model instead of training two models.

Now we are going to describe the training phase of ANN. We use two hidden layers whose depth $d_l = H$ is determined by trial and error [24]. For the input layer we have $d_l = d$ whilst for the output layer $d_l = N_T$ for $(WT1)_h$ and $d_l = N_M$ for $(WM)_h$. We consider N_t^T parameter tuples $\{\Xi_k\}_{k=1}^{N_t^T}$ and compute the temperature field $T_h(\Xi_k)$ by solving problem $(WT1)_h$ at each parameter tuple Ξ_k . Next, the temperature field $T_h(\Xi_k)$ is projected on the reduced basis space so to obtain the projected solution $T_h^{\pi}(\Xi_k)$ and corresponding degrees of freedom $\zeta_{T,\pi}(\Xi_k)$:

$$T_h^{\pi}(\Xi_k) = \underset{\psi_h^{rb} \in H_{r,h}^{1,rb}(\omega)}{\arg \min} ||T_h(\Xi_k) - \psi_h^{rb}||_{H_{r,h}^1(\omega)} = \sum_{i=1}^{N_T} \zeta_{T,\pi}^i(\Xi_k) \psi_h^i.$$
 (90)

Similarly, we consider N_t^M parameter tuples $\{\Xi_k\}_{k=1}^{N_t^M}$ and compute the displacement fields $\overrightarrow{u}_h(\Xi_k)$ by solving problem $(WM)_h$ at each parameter tuple Ξ_k . Next, the displacement field $\overrightarrow{u}_h(\Xi_k) \in \mathbb{U}_h$ is projected on the reduced basis space so to obtain the projected solution $\overrightarrow{u}_h^\pi(\Xi_k)$ and corresponding degrees of freedom $\zeta_{M,\pi}(\Xi_k)$:

$$\overrightarrow{u}_{h}^{\pi}(\Xi_{k}) = \underset{\overrightarrow{\phi}_{l}^{rb} \in \mathbb{U}_{l}^{rb}}{\arg\min} ||\overrightarrow{u}_{h}(\Xi_{k}) - \overrightarrow{\phi}_{h}^{rb}||_{\mathbb{U}_{h}} = \sum_{i=1}^{N_{M}} \zeta_{M,\pi}^{i}(\Xi_{k}) \overrightarrow{\phi}_{h}^{i}. \tag{91}$$

So we consider two collections of (known) training input-desidered output pairs, $\{\Xi_k, \zeta_{T,\pi}(\Xi_k)\}_{k=1}^{N_t^T}$ and $\{\Xi_k, \zeta_{M,\pi}(\Xi_k)\}_{k=1}^{N_t^M}$. The goal is to approximate the functions f_T and f_M that map these training input-desidered output pairs. After training the two ANNs, we consider them as black boxes that can then be used to compute the POD coefficients related to a new parameter instance Ξ^* .

We split the full order data into two parts: one to be used for training and one to be used for validation. While the training data are used to adjust weights and biasing parameters of the ANN, the validation data are used to measure its accuracy. A common issue is that ANN may perform better on training data but may not perform well on data other than training data. To avoid this overfitting phenomenon, we use the early stopping criteria [22]: the training is stopped

when the the mean squared error

$$\epsilon_{T} = \frac{\sum_{i=1}^{N_{T}} \left(\zeta_{T,\pi}^{i}(\Xi_{k}) - \zeta_{T}^{i}(\Xi_{k}) \right)^{2}}{N_{T}} ,$$

$$\epsilon_{M} = \frac{\sum_{i=1}^{N_{M}} \left(\zeta_{M,\pi}^{i}(\Xi_{k}) - \zeta_{M}^{i}(\Xi_{k}) \right)^{2}}{N_{M}} ,$$
(92)

as measured on validation data starts to increase.

7.3. Validation of MOR

We use a mesh of $\hat{\omega}$ containing 8887 triangular elements and 4608 vertices. The minimum mesh size is 0.047 m and the maximum one is 0.16 m. Its minimum quality is $q_e = 0.25$ (eq. 56). Notice that we use a coarser mesh with respect to the one used for the FOM benchmark tests in Sec. 6.1. Such a choice is justified by the fact that the FOM solution is required to be solved at many parameters values, so using a fine mesh can be very costly and make prohibitive the collection of the high-fidelity database.

The ranges of physical and geometrical parameters for training and testing are reported in Table 3. Concerning ANN, the training data are related to the 70% of the total data provided by the full order model whilst the remaining 30% is used for the validation.

Parameter	Minimum value	Maximum value
t_0	2.3	2.4
t_1	0.5	0.7
t_2	0.5	0.7
<i>t</i> ₃	0.4	0.6
t_4	3.05	3.35
D_0	13.5	14.5
D_1	8.3	8.7
D_2	8.8	9.2
D_3	9.8	10.2
D_4	10.4	10.8
k	9.8	10.2
μ	1.9e9	2.5e9
λ	1.2e9	1.8e9
α	0.8e-6	1.2e-6

Table 3: Parameters ranges used for MOR training and testing.

The accuracy of our MOR approach is quantified by the relative error defined as follows

$$\epsilon_{rel,X_h} = \frac{||X_h - X_h^{rb}||}{||X_h||},\tag{93}$$

where X_h and X_h^{rb} are the finite element solution and the corresponding reduced basis solution, respectively. $||\cdot||$ is the relevant norm $(||\cdot||_{H^1_{r,h}(\omega)})$ and $||\cdot||_{\mathbb{U}_h}$. We consider the projection error,

$$\epsilon_{proj,X_h} = \frac{||X_h - X_h^{\pi}||}{||X_h||}, \qquad (94)$$

as benchmark for the relative error.

7.3.1. Thermal model

We consider four experiments that differ in terms of kind (physical and/or geometrical) and number of the parameters considered:

- experiment (i): 1 physical parameter: $\Xi = \{k\}$.
- experiment (ii): 1 physical parameter and 3 geometric parameters: $\Xi = \{k, t_0, D_2, D_4\}$.
- experiment (iii): 1 physical parameter and 6 geometric parameters: $\Xi = \{k, t_0, t_2, t_4, D_0, D_2, D_4\}$.
- experiment (iv): 1 physical parameter and all (10) geometric parameters: $\Xi = \{k, t_0, t_1, t_2, t_3, t_4, D_0, D_1, D_2, D_3, D_4\}$.

Regarding the computation of POD space, for *experiment* (*i*), 50 FOM snapshots were considered while for the other ones 1000. The eigenvalues decay is shown in Fig. 13. We see that the decay related to the experiment (iv) is the slowest. This is due to the fact that in the experiment (iv) we consider a larger number of parameters, so the system exhibits a greater complexity, and the modal content is more wide.

Fig. 14 shows the relative error (93) both for POD-ANN, related to different values of the number of samples provided by the full order model n_{tr} and depth of hidden layers H, and POD-G. We also report the projection error (94). We observe that the performance of the POD-ANN method crucially depends on the values of n_{tr} and H. As expected, if we expand the training set and increase the depth of hidden layers, we obtain more accurate predictions when the number of parameters considered starts to get significative (experiments (iii) and (iv)). Unlike [24], we observe that the POD-G method results to be in general more accurate than the POD-ANN method. This could be justified by considering that in the nonlinear framework the affine expansion could not be enforced and an Empirical Interpolation Method (EIM) [4] is used within the POD-G approach. Its implementation introduces interpolation error during the assembling of the reduced equations system by significantly affecting the accuracy of the POD-G method.

Illustrative representations of the computed FOM and MOR are displayed in Fig. 15 related to the experiment (iv) for the parameters tuple

$$\Xi = \{2.365, 0.6, 0.6, 0.5, 3.2, 14.10, 8.50, 9.2, 9.9, 10.6, 10\}.$$

We use 4 POD basis. The POD-ANN solution was computed with $n_{tr} = 4500$ and H = 70. As we can see from Fig. 15, both MOR approaches are able to provide a good reconstruction of the temperature field.

We conclude by proving some information about the efficiency of our MOR approach. We report in Table 4 the online time related to the POD-G and POD-ANN methods for all the experiments carried out. As can be seen, the online time of POD-G method increases significantly in presence of geometric parameters by moving from 7e - 4 s (experiment (i)) to 1.3/1.5e - 2 s (experiment (ii)-(iv)). On the other hand, the time taken by POD-ANN online stage remains relatively constant for all the experiments under investigation, around 5e - 4. So the computational efficiency of POD-ANN is much higher, of almost two order of magnitude, than POD-G when geometrical parametrization is considered.

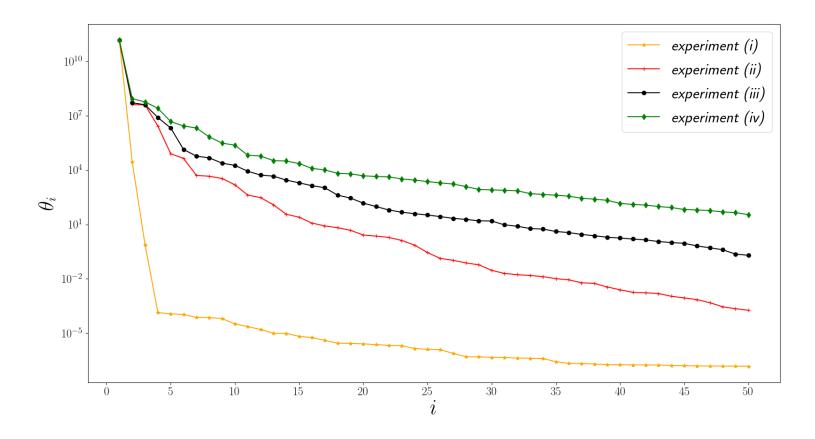


Figure 13: Thermal model: eigenvalues decay for all the experiments considered.

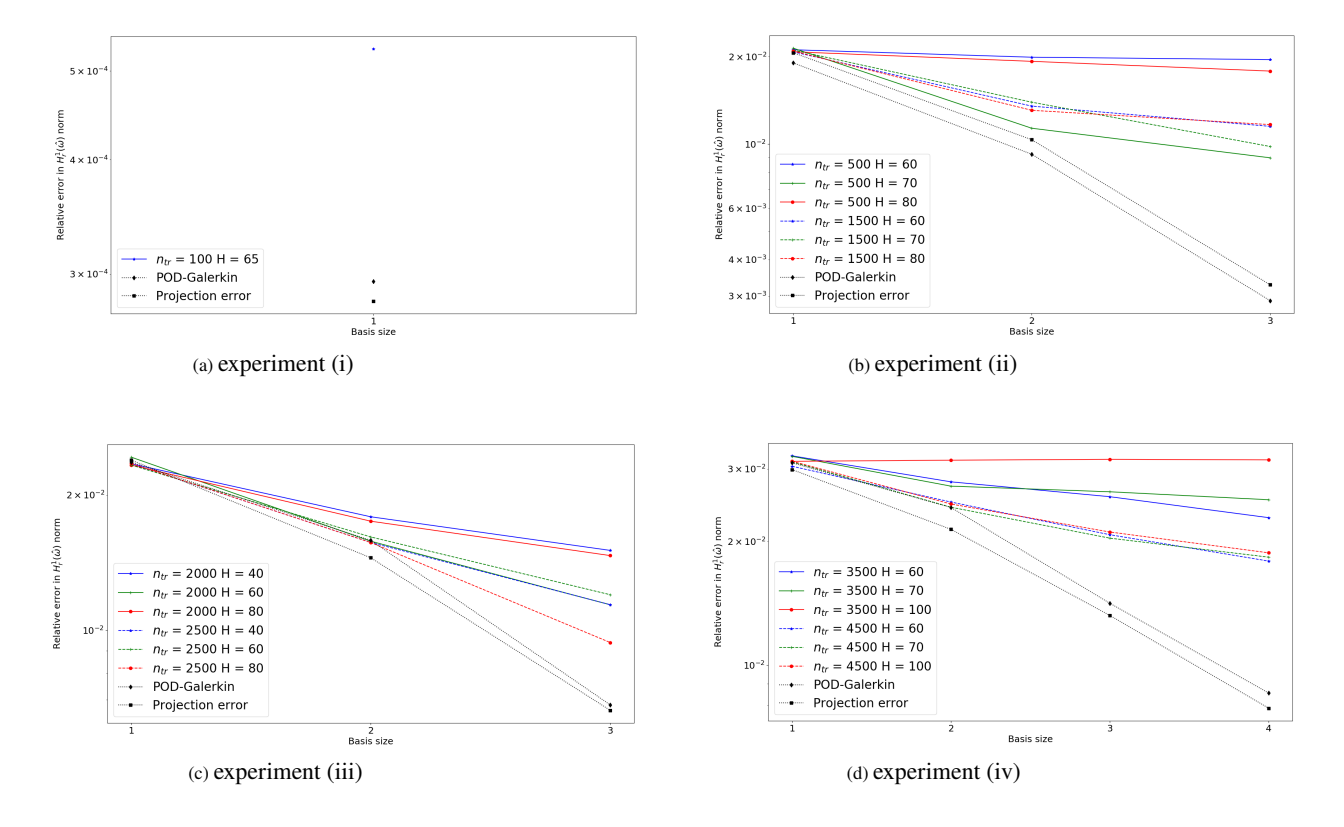


Figure 14: Thermal model: error analysis for POD-G and POD-ANN for all the experiments carried out.

	Basis size	POD-G	POD-ANN
experiment (i)	1	7e-4	4.9e-4
experiment (ii)	3	1.3e-2	4.8e-4
experiment (iii)	3	1.5e-2	4.9e-4
experiment (iv)	4	1.3e-2	5.1e-4

Table 4: Thermal model: online time (in s) for all the experiments under investigation. Concerning POD-ANN, we use $n_{tr} = 100$, H = 65 for the experiment (i), $n_{tr} = 500$, H = 70 for the experiment (ii) and $n_{tr} = 4500$, H = 70 for the experiment (iv).

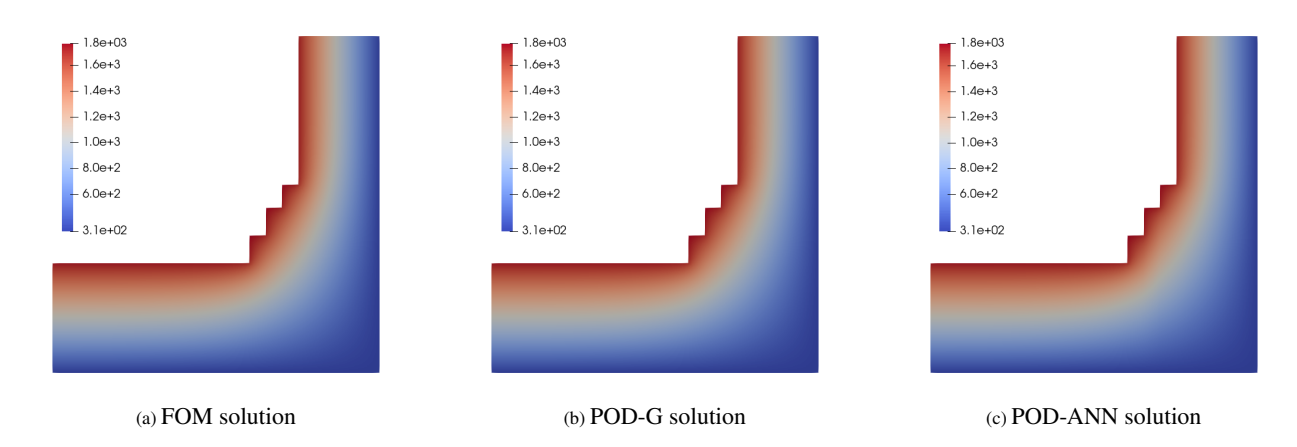


Figure 15: Thermal model: comparison between the temperature field (in K) computed by the FOM and by the POD-G and POD-ANN methods related to the experiment (iv) for $\Xi = \{2.365, 0.6, 0.6, 0.5, 3.2, 14.10, 8.50, 9.2, 9.9, 10.6, 10\}$. We consider 4 POD modes. For POD-ANN, we set $n_{tr} = 4500$ and H = 70.

7.3.2. Mechanical model

We remark that for POD-ANN we refer to the $(WM)_h$ model, whilst we consider $(WM1)_h$ and $(WM2)_h$ models for POD-G. As done for the thermal model, we consider four different experiments having different kinds and numbers of parameters:

- experiment (i): 4 physical parameters: $\Xi = \{k, \mu, \lambda, \alpha\}$.
- experiment (ii): 4 physical parameters and all 3 geometric parameters: $\Xi = \{k, \mu, \lambda, \alpha, t_0, D_2, D_4\}$.
- experiment (iii): 4 physical parameters and 6 geometric parameters: $\Xi = \{k, \mu, \lambda, \alpha, t_0, t_2, t_4, D_0, D_2, D_4\}$.
- experiment (iv): 4 physical parameters and all (10) geometric parameters: $\Xi = \{k, \mu, \lambda, \alpha, t_0, t_1, t_2, t_3, t_4, D_0, D_1, D_2, D_3, D_4\}.$

For all the experiments, the POD space was computed by considering 1000 snapshots. The eigenvalue plot is shown in Figure 16. Like the thermal model, we observe that the experiment (iv), characterized by the larger number of parameters, shows the lowest decay. On the other hand, as expected, among the different mechanical models we consider, the model $(WM)_h$ exhibits the slowest eigenvalues decay including it both thermal and mechanical effects.

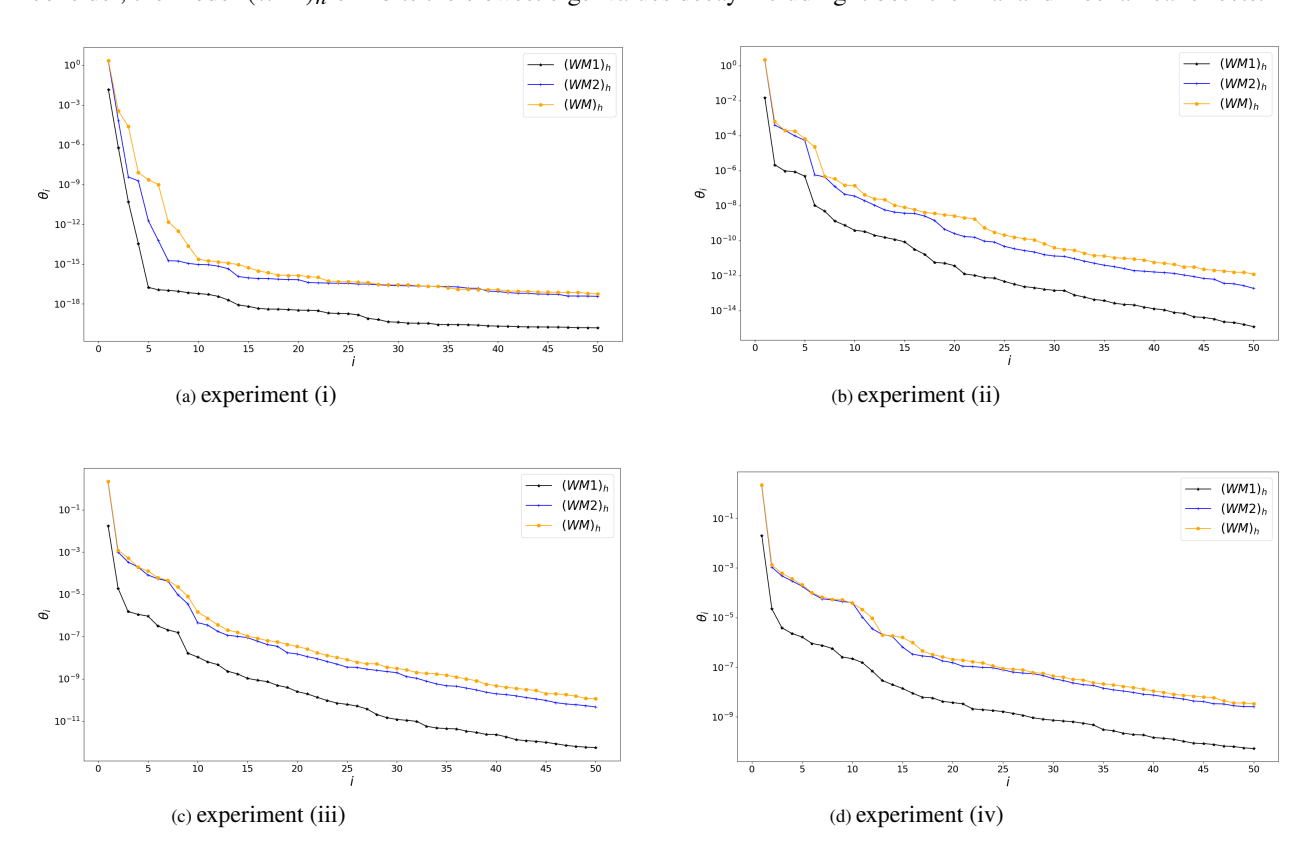


Figure 16: Mechanical model: eigenvalues decay for all the experiments considered.

Figure 17 shows the relative error (93) both for POD-ANN and POD-G. The projection error (94) is also depicted. As observed for the thermal model, POD-G is able to provide more accurate results with respect to POD-ANN.

Figure 18 shows the qualitative comparison between the computed FOM and MOR related to the experiment (iv) for the parameters tuple

```
\Xi = \{2.365, 0.6, 0.6, 0.5, 3.2, 14.10, 8.50, 9.2, 9.9, 10.6, 10, 2.08e9, 1.39e9, 1e - 6\}.
```

We use 7 POD basis. The POD-ANN solution was computed with $n_{tr} = 2500$ and H = 130. We could observe that both MOR approaches are able to provide a good reconstruction of the displacement field.

Finally, we briefly discuss the efficiency of our MOR approach. We report in Table 5 the online time related to the POD-G and POD-ANN methods for all the experiments carried out. Like the thermal model, the online time of POD-G method increases significantly in presence of geometric parameters by moving from 8e - 4 s (experiment (i)) to 2.6/6.9e - 2 s (experiments (ii)-(iv)) for the model $(WM1)_h$ and from 4.5e - 2 s (experiment (ii) to 1.9/2.6e - 1 s (experiments (ii)-(iv)) for the model $(WM2)_h$. We could observe that the online time taken by the model $(WM2)_h$ is significantly greater than that taken by the model $(WM1)_h$. This is expected because for the model $(WM2)_h$ a reduced basis approximation of temperature needs to be computed due to the thermo-mechanical coupling. On the other hand, the POD-ANN, that does not need reduced basis approximation of temperature thanks to its non intrusive nature, is able to provide a higher computational efficiency. Moreover, like the thermal model, the POD-ANN online time remains relatively constant for all the experiments under investigations, around 5e - 4, by showing a low sensitivity at varying of the kind and number of parameters considered.

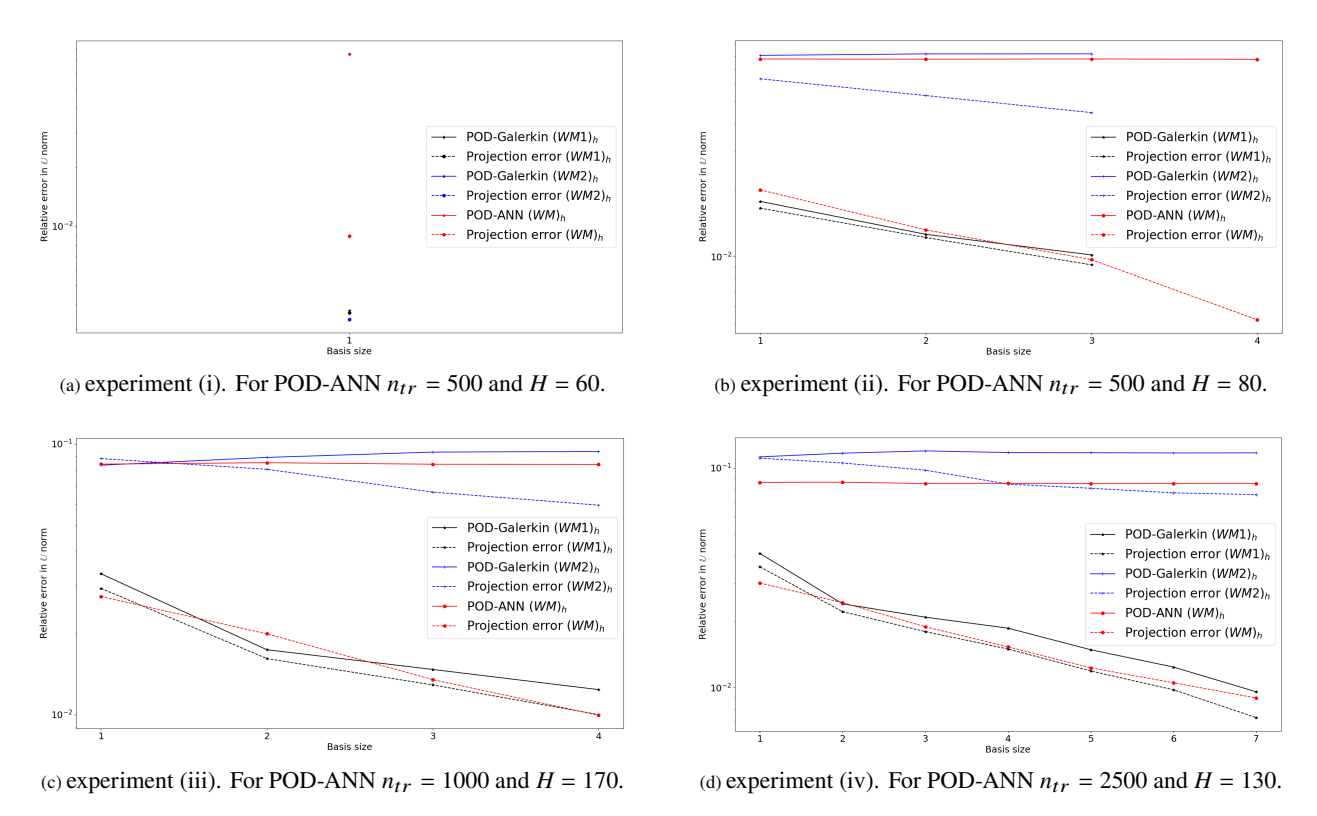


Figure 17: Mechanical model: error analysis for POD-G and POD-ANN for all the experiments considered.

	Basis size	POD-G $(WM1)_h$	POD-G $(WM2)_h$	POD-ANN $(WM)_h$
experiment (i)	1	8e-4	4.5e-2	6.7e-4
experiment (ii)	3	2.6e-2	1.9e-1	5.3e-4
experiment (iii)	4	5.4e-2	2.1e-1	5.2e-4
experiment (iv)	7	6.9e-2	2.6e-1	4.9e-4

Table 5: Mechanical model: online time (in s) for all the experiments under investigation. Concerning POD-ANN, we use $n_{tr} = 500$, H = 60 for the experiment (i), $n_{tr} = 500$, H = 80 for the experiment (ii), $n_{tr} = 1000$, H = 170 for the experiment (iii) and $n_{tr} = 2500$, H = 130 for the experiment (iv).

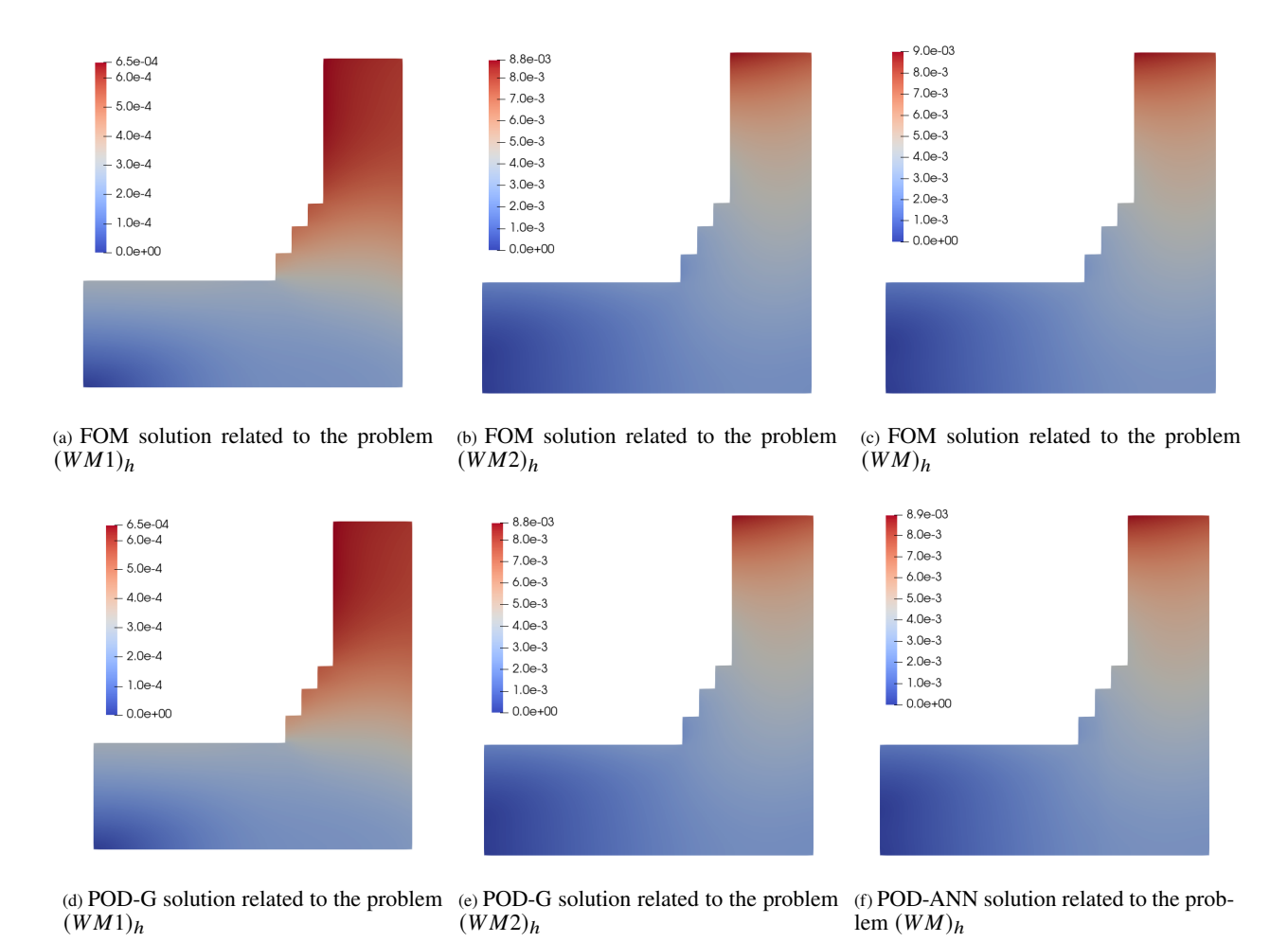


Figure 18: Mechanical model: comparison between the displacement (in m) computed by FOM and by the POD-G and POD-ANN methods related to the experiment (iv) for $\Xi = \{2.365, 0.6, 0.6, 0.5, 3.2, 14.10, 8.50, 9.2, 9.9, 10.6, 10, 2.08e9, 1.39e9, 1e - 6\}$. We consider 7 POD modes. For POD-ANN, we set $n_{tr} = 2500$ and H = 130.

8. Some concluding remarks

In this work we propose a computational pipeline to obtain fast and reliable numerical simulations for one-way coupled steady state linear thermo-mechanical problems in a finite element environment. The test case is referred to a relevant industrial problem related to the investigation of the thermo-mechanical phenomena occurring in blast furnace heart walls. After introducing the main theoretical features of FOM, we detect customized benchmarks for the validation of its numerical implementation. Then we present our MOR framework: we apply POD for the computation of reduced basis space whilst for the evaluation of the modal coefficients we use two different methodologies, the one based on a classic Galerkin projection (POD-G) and the other one based on artificial neural networks (POD-ANN). We found that POD-G is generally more accurate than POD-ANN although POD-ANN exhibits a very higher efficiency, especially when geometric parameters are considered.

We believe that insights given in this work could help to develop advanced numerical tools in order to deal with complex industrial problems. As a follow-up of this work, we are going to enhance training capacity of the deep learning methods and move towards more complex thermo-mechanical problems involving heterogeneity, orthotropy and non-linearity.

Acknowledgements

We are grateful to Dr. Federico Pichi (SISSA mathLab) for insights and crucial support in the numerical implementation of artificial neural network.

We would like to acknowledge the financial support of the European Union under the Marie Sklodowska-Curie Grant Agreement No. 765374. We also acknowledge the partial support by the European Union Funding for Research and Innovation - Horizon 2020 Program - in the framework of European Research Council Executive Agency: Consolidator Grant H2020 ERC CoG 2015 AROMA-CFD project 681447 "Advanced Reduced Order Methods with Applications in Computational Fluid Dynamics" and INDAM-GNCS project "Advanced intrusive and non-intrusive model order reduction techniques and applications", 2019. This work was also partially supported by FEDER and Xunta de Galicia [grant numbers ED431C 2017/60, ED431C 2021/15], and the Agencia Estatal de Investigación [PID2019-105615RB-I00/AEI/10.13039/501100011033].

This work has focused exclusively on civil applications. It is not to be used for any illegal, deceptive, misleading or unethical purpose or in any military applications. This includes any application where the use of this work may result in death, personal injury or severe physical or environmental damage.

References

- [1] Alnæs, M.S., Blechta, J., Hake, J., Johansson, A., Kehlet, B., Logg, A., Richardson, C., Ring, J., Rognes, M.E., Wells, G.N., 2015. The fenics project version 1.5. Archive of Numerical Software 3.
- [2] Amsallem, D., Cortial, J., Carlberg, K., Farhat, C., 2009. A method for interpolating on manifolds structural dynamics reduced-order models. International Journal for Numerical Methods in Engineering 80, 1241–1258.
- [3] Bader, E., Kärcher, M., Grepl, M., Veroy, K., 2016. Certified reduced basis methods for parametrized distributed elliptic optimal control problems with control constraints. SIAM Journal on Scientific Computing 38, A3921–A3946.
- [4] Barrault, M., Maday, Y., Nguyen, N.C., Patera, A.T., 2004. An 'empirical interpolation' method: application to efficient reduced-basis discretization of partial differential equations. Comptes Rendus Mathematique 339, 667–672.
- [5] Benner, P., Gugercin, S., Willcox, K., 2015a. A survey of projection-based model reduction methods for parametric dynamical systems. SIAM Review 57, 483–531.
- [6] Benner, P., Herzog, R., Lang, N., Riedel, I., Saak, J., 2019. Comparison of model order reduction methods for optimal sensor placement for thermo-elastic models. Engineering Optimization 51, 465–483.
- [7] Benner, P., Ohlberger, M., Patera, A., Rozza, G., Urban, K., 2015b. A survey of projection-based model reduction methods for parametric dynamical systems. SIAM Review 57, 483–531.
- [8] Benner, P., Schilders, W., Grivet-Talocia, S., Quarteroni, A., Rozza, G., Silveira, L.M. (Eds.), 2020. Model Order Reduction. De Gruyter.
- [9] Brezis, H., 2010. Functional Analysis, Sobolev Spaces and Partial Differential Equations. Universitext, Springer New York.
- [10] Brulin, J., Rekik, A., Blond, E., Josserand, L., Gasser, A., Roulet, F., 2011. Thermomechanical modelling of a blast furnace hearth, UNITECR'11, Kyoto, Japan. pp. CD–ROM. hal-00651546.
- [11] Cameron, I., Sukhram, M., Lefebvre, K., Davenport, W., 2019. Blast furnace ironmaking: Analysis, control, and optimization, Elsevier.
- [12] Bermúdez de Castro, A., 2005. Continuum thermomechanics. Progress in Mathematical Physics 43.
- [13] Chen, W., Wang, Q., Hesthaven, J.S., Zhang, C., 2021. Physics-informed machine learning for reduced-order modeling of nonlinear problems. Journal of Computational Physics 446, 110666.
- [14] Demo, N., Tezzele, M., Rozza, G., 2019. A non-intrusive approach for the reconstruction of pod modal coefficients through active subspaces. Comptes Rendus Mécanique 347, 873–881. Data-Based Engineering Science and Technology.

- [15] Demuth, H.B., Beale, M.H., Jesús, O.D., Hagan, M.T., 2014. Neural network design. Cambridge University Press.
- [16] FEniCS, URL: www.fenicsproject.org. Accessed: 04-December-2021.
- [17] Geerdes, M., Chaigneau, R., Lingiardi, O., 2020. Modern Blast Furnace Ironmaking: An Introduction (Fourth Edition, 2020). IOS Press.
- [18] Gurtin, M., 1981. An Introduction to Continuum Mechanics. Academic Press.
- [19] Gurtin, M.E., Fried, E., Anand, L., 2010. The Mechanics and Thermodynamics of Continua. Cambridge University Press.
- [20] Guérin, N., Thorin, A., Thouverez, F., Legrand, M., Almeida, P., 2018. Thermomechanical Model Reduction for Efficient Simulations of Rotor-Stator Contact Interaction. Journal of Engineering for Gas Turbines and Power 141.
- [21] Haasdonk, B., 2017. Reduced Basis Methods for Parametrized PDEs—A Tutorial Introduction for Stationary and Instationary Problems. chapter 2. pp. 65–136.
- [22] Haykin, S., 2009. Neural Networks and Learning Machines. Number v. 10 in Neural networks and learning machines, Prentice Hall.
- [23] Hernández-Becerro, P., Spescha, D., Wegener, K., 2021. Model order reduction of thermo-mechanical models with parametric convective boundary conditions: focus on machine tools. Computational Mechanics 67, 167–184.
- [24] Hesthaven, J., Ubbiali, S., 2018. Non-intrusive reduced order modeling of nonlinear problems using neural networks. Journal of Computational Physics 363, 55 78.
- [25] Hesthaven, J.S., Rozza, G., Stamm, B., 2015. Certified Reduced Basis Methods for Parametrized Partial Differential Equations. SpringerBriefs in Mathematics, Springer International Publishing.
- [26] Hlaváček, I., 1989. Korn's inequality uniform with respect to a class of axisymmetric bodies. Aplikace Matematiky 34, 146–154.
- [27] Hlaváček, I., 1989. Shape optimization of elastic axisymmetric bodies. Aplikace matematiky 34, 225–245.
- [28] Hoang, K.C., Kim, T.Y., 2017. Fast and accurate two-field reduced basis approximation for parametrized thermoelasticity problems. Finite Elements in Analysis and Design 141, 96–118.
- [29] Huynh, D., Patera, A., 2007. Reduced basis approximation and a posteriori error estimation for stress intensity factors. International Journal for Numerical Methods in Engineering 72, 1219–1259.
- [30] Kingma, D.P., Ba, J., 2015. Adam: A method for stochastic optimization, 3rd International Conference on Learning Representations (ICLR). arXiv:1412.6980.
- [31] Li, H., 2011. Finite element analysis for the axisymmetric laplace operator on polygonal domains. J. Computational Applied Mathematics 235, 5155–5176.
- [32] Li, Z., Kovachki, N., Azizzadenesheli, K., Liu, B., Bhattacharya, K., Stuart, A., Anandkumar, A., 2020. Neural operator: Graph kernel network for partial differential equations. arXiv:2003.03485.
- [33] Li, Z., Kovachki, N., Azizzadenesheli, K., Liu, B., Bhattacharya, K., Stuart, A., Anandkumar, A., 2021. Fourier neural operator for parametric partial differential equations. arXiv:2010.08895.
- [34] Necas, J., 1967. Les Methodes Directes en Theorie Des Equations Elliptiques Jindrich Necas. Masson.
- [35] Paszke, A., Gross, S., Massa, F., Lerer, A., Bradbury, J., Chanan, G., Killeen, T., Lin, Z., Gimelshein, N., Antiga, L., Desmaison, A., Kopf, A., Yang, E., DeVito, Z., Raison, M., Tejani, A., Chilamkurthy, S., Steiner, B., Fang, L., Bai, J., Chintala, S., 2019. Pytorch: An imperative style, high-performance deep learning library, in: Wallach, H., Larochelle, H., Beygelzimer, A., d'Alché-Buc, F., Fox, E., Garnett, R. (Eds.), Advances in Neural Information Processing Systems 32. Curran Associates, Inc., pp. 8024–8035.

- [36] Pichi, F., Ballarin, F., Rozza, G., Hesthaven, J.S., 2021. An artificial neural network approach to bifurcating phenomena in computational fluid dynamics. arXiv:2109.10765.
- [37] PyTorch, URL: www.pytorch.org. Accessed: 04-December-2021.
- [38] Quarteroni, A., Manzoni, A., Negri, F., 2016. Reduced Basis Methods for Partial Differential Equations. Number v. 1 in La Matematica per il 3+2, Springer International Publishing.
- [39] Raissi, M., Perdikaris, P., Karniadakis, G., 2019. Physics-informed neural networks: A deep learning framework for solving forward and inverse problems involving nonlinear partial differential equations. Journal of Computational Physics 378, 686–707.
- [40] Raissi, M., Yazdani, A., Karniadakis, G.E., 2020. Hidden fluid mechanics: Learning velocity and pressure fields from flow visualizations. Science 367, 1026–1030.
- [41] RBniCS, URL: www.rbnicsproject.org. Accessed: 04-December-2021.
- [42] Rojas, R., 1996. Neural Networks: A Systematic Introduction. Springer-Verlag, Berlin, Heidelberg.
- [43] Rozza, G., Huynh, D., Patera, A., 2007. Reduced basis approximation and a posteriori error estimation for affinely parametrized elliptic coercive partial differential equations. Archives of Computational Methods in Engineering 15.
- [44] San, O., Maulik, R., Ahmed, M., 2019. An artificial neural network framework for reduced order modeling of transient flows. Communications in Nonlinear Science and Numerical Simulation 77, 271–287.
- [45] Schilders, W., 2008. Introduction to Model Order Reduction. Springer Berlin Heidelberg, Berlin, Heidelberg. pp. 3–32.
- [46] Schilders, W.H.A., Lutowska, A., 2014. A Novel Approach to Model Order Reduction for Coupled Multiphysics Problems. Springer International Publishing, Cham. pp. 1–49.
- [47] Sinha, T., Sikka, K., Lall, R., 2021. Artificial neural networks and bayesian techniques for flip-chip package thermo-mechanical analysis, 2021 IEEE 71st Electronic Components and Technology Conference (ECTC), pp. 1442–1449.
- [48] Swartling, M., Sundelin, B., Tilliander, A., Jönsson, P.G., 2010. Heat transfer modelling of a blast furnace hearth. steel research international 81, 186–196.
- [49] Vizzaccaro, A., Givois, A., Longobardi, P., Shen, Y., Deü, J.F., Salles, L., Touzé, C., Thomas, O., 2020. Non-intrusive reduced order modelling for the dynamics of geometrically nonlinear flat structures using three-dimensional finite elements. Computational Mechanics 66, 1293–1319.
- [50] Vázquez-Fernández, S., García-Lengomín Pieiga, A., Lausín-Gónzalez, C., Quintela, P., 2019. Mathematical modelling and numerical simulation of the heat transfer in a trough of a blast furnace. International Journal of Thermal Sciences 137, 365 374.
- [51] Wang, Q., Hesthaven, J.S., Ray, D., 2019. Non-intrusive reduced order modeling of unsteady flows using artificial neural networks with application to a combustion problem. Journal of Computational Physics 384, 289–307.
- [52] Zhang, G., Eddy Patuwo, B., Y. Hu, M., 1998. Forecasting with artificial neural networks:: The state of the art. International Journal of Forecasting 14, 35–62.
- [53] Zhang, S., Oskay, C., 2017. Reduced order variational multiscale enrichment method for thermo-mechanical problems. Computational Mechanics 59, 887–907.
- [54] Zienkiewicz, O.C., Taylor, R.L., Zhu, J.Z., 2005. The Finite Element Method: Its Basis and Fundamentals. 6 ed., Butterworth-Heinemann.